A Nonlinear Inversion Method for 3D-Electromagnetic Imaging Using Adjoint Fields

O. Dorn * H. Bertete-Aguirre † J.G. Berryman ‡
G.C. Papanicolaou §

September 11, 1999

Abstract

Electromagnetic Imaging is modeled as an inverse problem for the 3D system of Maxwell's equations of which the isotropic conductivity distribution in the domain of interest has to be reconstructed. The main application we have in mind is the monitoring of conducting contaminant plumes out of surface and borehole electromagnetic imaging data. The essential feature of the method developed here is the use of adjoint fields for the reconstruction task, combined with a splitting of the data into smaller groups which define subproblems of the inversion problem. The method works iteratively, and can be considered as a nonlinear generalization of the Algebraic Reconstruction Technique (ART) in x-ray tomography. Starting out from some initial guess for the conductivity distribution, an update for this guess is computed by solving one forward and one adjoint problem of the 3D Maxwell system at a time. Numerical experiments are performed for a layered background medium in which one or two localized (3D) inclusions are immersed. These have to be monitored out of surface to borehole and cross-borehole EM data. We show that the algorithm is able to recover a single inclusion in the earth which has high contrast to the background, and to distinguish between two separated inclusions in the earth given certain borehole geometries.

*Department of Mathematics, Stanford University, Stanford CA 94305, dorn@math.stanford.edu
†Lawrence Livermore National Laboratory, P.O.Box 808, L-206, Livermore CA 94551-9900, hba@llnl.gov
‡Lawrence Livermore National Laboratory, P.O.Box 808, L-200, Livermore CA 94551-9900, berryman1@llnl.gov
§Department of Mathematics, Stanford University, Stanford CA 94305, papanico@math.stanford.edu

Contents

1 Introduction

The solid earth and certain pore fluids (such as hydrocarbons) are comparatively poor electrical conductors, while other pore fluids (such as brines) are good electrical conductors. If we wish to image the shape of conducting fluid plumes underground (as we might, *e.g.*, for environmental cleanup purposes), one practical way of doing so is to make either electrical or electromagnetic measurements between boreholes (when two or more boreholes are available) or between borehole and surface arrays. One popular electromagnetic method of imaging without the need for boreholes is Ground Penetrating Radar (Davis and Anan [13]; Fisher *et al.* [17]), normally operating in the radio to microwave range of frequencies. GPR methods for imaging conductivity use comparatively high frequencies ($\geq$ 100 MHz) in order to have a signal that propagates through the Earth as a wave. The main practical difficulty with GPR imaging is that at these frequencies its depth of penetration is usually no deeper than about 5 meters into the Earth in dry soil/sand, while maximum depths of less than 1-2 meters are more typical in wet earth due to high local wave attenuation.

Electromagnetic induction tomography is a promising new tool for imaging electrical conductivity variations in the earth (Wilt *et al.* [33],[34]) with a depth of investigation greater than GPR. The source is a magnetic field generated by currents in wire coils. This source field is normally produced in one borehole, while the received signals are the measured small changes in magnetic field in another, more distant borehole. The method may also be used successfully in combination with surface sources and receivers. The goal of this procedure is to image electrical conductivity variations in the earth, much as x-ray tomography is used to image density variations through cross-sections of the body. However, the fields tend to diffuse rather than propagate as waves in this frequency band (from about 1 to 20 kHz) and the inversion techniques are therefore very different from those for GPR. Although field techniques have been developed and applied previously to collection of such EM data, the algorithms for inverting the magnetic field data to produce the desired images of electrical conductivity have not kept pace. The current state of the art in electromagnetic data inversion (Alumbaugh and Morrison [1],[2]) is based on the Born/Rytov approximation (requiring a low contrast assumption), even though it is known that conductivity variations range over several orders of magnitude and therefore require nonlinear analysis. Other recent work on inversion for this problem has been presented by Habashy *et al.* [18] and by Newman and Alumbaugh [23]. The ultimate goal of the work presented here is therefore to produce better images of electrically conducting fluids underground by using robust inversion techniques over greater distances and higher contrasts than were previously possible.

Although other technologies, such as Electrical Resistance Tomography or ERT (Berryman and Kohn [5]; Daily *et al.* [12]; Ramirez *et al.* [25]; Borcea [6]; Borcea *et al.* [7]) can produce electrical conductivity images at a useful spatial scale, the advantage of the ElectroMagnetic Induction Tomography or EMIT is that we can make use of existing monitoring wells and the surface to do our imaging. Since signals are transmitted and received inductively, we do not need to make ground contact (no ground penetrating electrodes); the technology is therefore relatively noninvasive. Furthermore, all conductors present can in principle be imaged using the EMIT technique, whereas ERT can only image those conductors maintaining a continuous electrical current path between the source and/or receiver electrodes. There is also the important potential advantage for both techniques that multiple frequencies can be employed to improve the imaging capability.

We present a new approach to the inverse problem of electromagnetic induction tomography. This method is based on the so-called "adjoint technique," which (for the present application) has the very useful property that the inverse problem can be solved approximately by making two uses of the same forward modeling code. Using a somewhat oversimplified description of our technique, the updates to the electrical conductivity are obtained by first making one pass through the code using the latest best guess of the nature of the conducting medium, and then another pass with the adjoint operator applied to the differences in computed and measured data. Then the results of these two calculations are combined to determine updates to the original conductivity model. The resulting procedure is iterative and can be applied successively to parts of the data, *e.g.*, data associated with one transmitter location can be used to update the model before other transmitter locations are considered. This procedure has several of the same advantages as wave equation migration in reflection seismology (Claerbout [11]) and is also related to recent methods in electromagnetic migration introduced by Zhdanov *et al.* [37].

In Section 2 we present the basic equations of electromagnetics in a form convenient for development of the adjoint technique. In Section 3 we reformulate the problem in terms of operators and the Adjoint Field Method is presented in Section 4. Section 5 is a summary of the numerical method used in the EM solver for both modeling and inversion. In Section 6 we describe in detail the numerical reconstructions that we have carried out. The final section summarizes our results and indicates some directions for future research.

2 The physical experiment

2.1 Maxwell's equations

We consider the system of time-harmonic Maxwell's equations in three spatial dimensions

$$\nabla \times \mathbf{H}(\mathbf{x}) - (i\omega\epsilon(\mathbf{x}) + \sigma(\mathbf{x}))\,\mathbf{E}(\mathbf{x}) = \mathbf{J}(\mathbf{x}) \tag{1}$$

$$\nabla \times \mathbf{E}(\mathbf{x}) + i\omega\mu(\mathbf{x})\,\mathbf{H}(\mathbf{x}) = \mathbf{M}(\mathbf{x}) \tag{2}$$

$$\nabla \cdot \epsilon\mathbf{E}(\mathbf{x}) = 0 \tag{3}$$

$$\nabla \cdot \mu\mathbf{H}(\mathbf{x}) = 0 \tag{4}$$

Here, $\mathbf{E}(\mathbf{x})$ and $\mathbf{H}(\mathbf{x})$ denote the electric and magnetic field, $\mathbf{J}(\mathbf{x})$ and $\mathbf{M}(\mathbf{x})$ the electric and magnetic source currents, and ω is the angular frequency, $\omega = 2\pi f$. The parameters describing the underlying medium are the electric conductivity $\sigma(\mathbf{x})$, the dielectric permittivity $\epsilon(\mathbf{x})$, and the magnetic permeability $\mu(\mathbf{x})$. We assume that all these parameters are strictly positive $\sigma(\mathbf{x}) > 0$, $\epsilon(\mathbf{x}) > 0$, and $\mu(\mathbf{x}) > 0$ in $\mathbb{R}^3$. We consider only isotropic media where all three parameters are described by 3D scalar fields. This assumption is introduced here for simplicity and is not necessary for the derivation of the inversion algorithm. We will discuss the more general case of inverse problems for anisotropic media in a forthcoming publication. Equations (3) and (4) indicate that there are no electric or magnetic space charges in the medium.

Equations (1)-(4) describe the propagation of an electromagnetic field which is generated by a (time-harmonic) source

$$\tilde{\mathbf{q}}(\mathbf{x},t) \;=\; \mathbf{q}(\mathbf{x})e^{i\omega t},$$

where we have defined the source distribution $\mathbf{q}(\mathbf{x})$ by

$$\mathbf{q}(\mathbf{x}) \;=\; \begin{pmatrix} \mathbf{J}(\mathbf{x}) \\ \mathbf{M}(\mathbf{x}) \end{pmatrix}. \tag{5}$$

We will use systematically the notation

$$\begin{aligned} \alpha \;&:=\; i\omega\mu, &(6)\\ \beta \;&:=\; i\omega\epsilon + \sigma. &(7) \end{aligned}$$

With the notation of (6),(7) we write (1),(2) as

$$\begin{aligned} \nabla\times\mathbf{H}(\mathbf{x}) - \beta(\mathbf{x})\,\mathbf{E}(\mathbf{x}) \;&=\; \mathbf{J}(\mathbf{x}), &(8)\\ \nabla\times\mathbf{E}(\mathbf{x}) + \alpha(\mathbf{x})\,\mathbf{H}(\mathbf{x}) \;&=\; \mathbf{M}(\mathbf{x}). &(9) \end{aligned}$$

This is the form of Maxwell's equations that we will use.

2.2 The measurements

We consider (8),(9) in the unbounded domain $\Omega = \mathbb{R}^3$ for p different sources $\mathbf{q}_j$, $j = 1,\ldots,p$. These sources might for example be magnetic dipole sources which have the form

$$\mathbf{q}_j^{\mathrm{dp}}(\mathbf{x}) \;=\; \begin{pmatrix} 0 \\ \mathbf{m}_j \end{pmatrix} \delta(\mathbf{x}-\mathbf{x}_j) \tag{10}$$

with complex constants $\mathbf{m}_j \in \mathbb{C}^3$ for $j = 1,\ldots,p$. Other choices are, however, possible.

We assume that equations (8),(9) provide a model for the propagation of the radiation caused by the sources $\mathbf{q}_j$, $j = 1,\ldots,p$, and we measure the magnetic components of these fields $\hat{M}_{jk} = \hat{\mathbf{H}}_j(d_{jk})$ for each source $\mathbf{q}_j$ and for m_j discrete detector positions d_{jk} , $k = 1,\ldots,m_j$. The total number of detectors m_j may vary with the source $\mathbf{q}_j$.

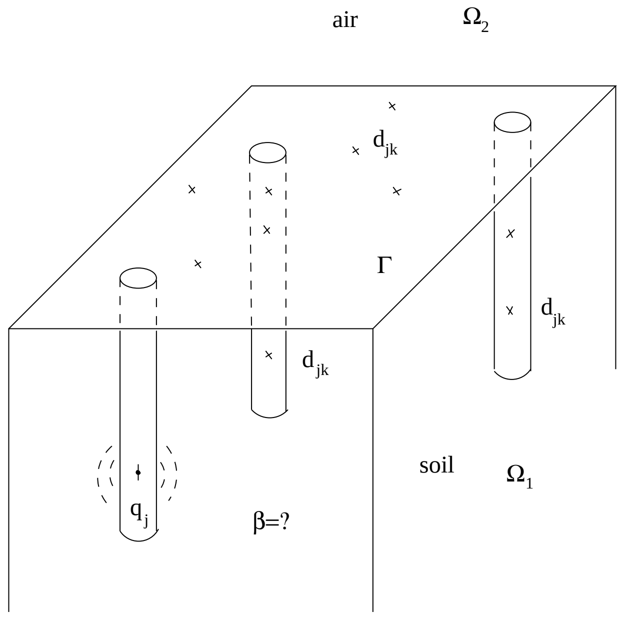

Figure 1: The figure shows a possible experimental setup. Three boreholes surround the area where we want to recover the conductivity. A z-directed dipole transmitter q_j is deployed in one of the boreholes, and data are gathered in the other boreholes and at the surface at positions d_{jk}, $k = 1, \ldots, m_j$. This is done for p different transmitter locations $j = 1, \ldots, p$. The real part of $\beta(x)$ corresponds to the isotropic conductivity distribution in the medium, and has to be reconstructed out of the data.

We denote by $\hat{\alpha}(\mathbf{x})$, $\hat{\beta}(\mathbf{x})$ the 'true' parameter distributions, and by

$$\hat{\mathbf{u}}_j = \begin{pmatrix} \hat{\mathbf{E}}_j(\mathbf{x}) \\ \hat{\mathbf{H}}_j(\mathbf{x}) \end{pmatrix}$$

the solution of equations (8),(9) with the parameters $\alpha = \hat{\alpha}$, $\beta = \hat{\beta}$ and with the source

$$\mathbf{q}_j = \begin{pmatrix} \mathbf{J}_j \\ \mathbf{M}_j \end{pmatrix}. \tag{11}$$

2.3 The inverse problem

In geophysical applications it is often the case that the coefficient $\hat{\alpha}$ does not vary significantly in the region of interest. We will therefore assume that $\hat{\alpha}$ is known in the whole domain Ω and will denote it by α.

The coefficient $\hat{\beta}$ is usually assumed to be known in some parts of Ω, for example in the air, and has to be reconstructed in the remaining part of the region. This prior information about $\hat{\beta}$ can be taken into account in the derivation of the inversion algorithm by expressing the function β as a sum of a known and an unknown part, which has to be recovered. To simplify the derivation, we will assume that we have to recover $\hat{\beta}$ in the whole domain Ω, from the measured data $\hat{\mathbf{H}}_j(d_{jk})$. The available prior information about $\hat{\beta}$ is taken into account in the numerical implementation of the method by restricting the updates in a suitable way.

The inverse problem is as follows. For each of the source distributions $(\mathbf{J}_j, \mathbf{M}_j)^T$, $j = 1, \ldots, p$, data $\hat{M}_{jk}$, $k = 1, \ldots, m_j$ are measured or are synthetically generated. We want to find a parameter distribution $\hat{\beta}$, such that for the solutions $(\hat{\mathbf{E}}_j, \hat{\mathbf{H}}_j)^T$ of

$$\nabla \times \hat{\mathbf{H}}_j - \hat{\beta}\,\hat{\mathbf{E}}_j = \mathbf{J}_j, \tag{12}$$

$$\nabla \times \hat{\mathbf{E}}_j + \alpha\,\hat{\mathbf{H}}_j = \mathbf{M}_j, \tag{13}$$

$j = 1, \ldots, p$, the magnetic field values at the detector positions d_{jk} coincide with the data

$$\hat{M}_{jk} = \hat{\mathbf{H}}_j(d_{jk}) \ , \quad k = 1, \ldots, m_j. \tag{14}$$

If there is no noise in the data then there may be many parameter distributions $\hat{\beta}$ that satisfy (14) so we have to select one using a regularization criterion. If there is noise, the usual case, then (14) can be satisfied only in the sense of minimizing the sum of the squares of the differences between the two sides.

We want to derive an efficient method for solving this inverse problem. For this purpose it is advantageous to introduce a slightly more formal description of the problem. We do this in the following section.

3 Operator formulation.

3.1 The function spaces

We define now the basic function spaces which are used throughout this paper. The main objective of this section is to introduce the inner products which will be used in the derivation of the adjoint of the linearized residual operator in section 4.8.

Let

$$\begin{aligned} F &:= L^2(\Omega) \\ U &:= \left\{ \begin{pmatrix} \mathbf{E}(\mathbf{x}) \\ \mathbf{H}(\mathbf{x}) \end{pmatrix} \; ; \; \mathbf{E}, \mathbf{H} \in [L^2(\Omega)]^3 \right\}, \\ Y &:= \left\{ \begin{pmatrix} \mathbf{J}(\mathbf{x}) \\ \mathbf{M}(\mathbf{x}) \end{pmatrix} \; ; \; \mathbf{J}, \mathbf{M} \in [L^2(\Omega)]^3 \right\}, \\ Z_j &:= \left\{ \begin{pmatrix} \eta \\ \xi \end{pmatrix} \; ; \; \eta, \xi \in (\mathbb{C}^3)^{m_j} \right\} \quad , j = 1, \ldots, p. \end{aligned}$$

Here, F is the space of parameters β, Y the space of sources $\mathbf{q}$, U the space of states $\binom{\mathbf{E}}{\mathbf{H}}$, and Z_j the space of measurements $\zeta = \binom{\eta}{\xi}$, which depends on the source $\mathbf{q}_j$.

We assume that U, Y, and Z_j are equipped with the following inner products

$$\left\langle \begin{pmatrix} \mathbf{E}_1 \\ \mathbf{H}_1 \end{pmatrix}, \begin{pmatrix} \mathbf{E}_2 \\ \mathbf{H}_2 \end{pmatrix} \right\rangle_{L^2} := \int_\Omega \mathbf{E}_1 \overline{\mathbf{E}_2} \, d\mathbf{x} + \int_\Omega \mathbf{H}_1 \overline{\mathbf{H}_2} \, d\mathbf{x},$$

where $\binom{\mathbf{E}_1}{\mathbf{H}_1}$, $\binom{\mathbf{E}_2}{\mathbf{H}_2}$ are some elements of U,

$$\left\langle \begin{pmatrix} \mathbf{J}_1 \\ \mathbf{M}_1 \end{pmatrix}, \begin{pmatrix} \mathbf{J}_2 \\ \mathbf{M}_2 \end{pmatrix} \right\rangle_{L^2} := \int_\Omega \mathbf{J}_1 \overline{\mathbf{J}_2} \, d\mathbf{x} + \int_\Omega \mathbf{M}_1 \overline{\mathbf{M}_2} \, d\mathbf{x},$$

where $\binom{\mathbf{J}_1}{\mathbf{M}_1}$, $\binom{\mathbf{J}_2}{\mathbf{M}_2}$ are some elements of Y and

$$\left\langle \begin{pmatrix} \eta_1 \\ \xi_1 \end{pmatrix}, \begin{pmatrix} \eta_2 \\ \xi_2 \end{pmatrix} \right\rangle_{Z_j} := \sum_{k=1}^{m_j} \eta_{1,k} \overline{\eta_{2,k}} + \sum_{k=1}^{m_j} \xi_{1,k} \overline{\xi_{2,k}},$$

where $\binom{\eta_1}{\xi_1}$, $\binom{\eta_2}{\xi_2}$ are some elements of Z_j. Bar denotes complex conjugate.

The space F is equipped with the usual inner product in $L_2(\mathbb{R}^3)$ and F, U, Y and Z_j are Hilbert spaces with these inner products.

3.2 The measurement operator

We write equations (8),(9) in system form

$$\Lambda_M(\beta) \, \mathbf{u} = \mathbf{q}, \tag{15}$$

with

$$\Lambda_M(\beta) := \begin{pmatrix} -\beta & \nabla\times \\ \nabla\times & \alpha \end{pmatrix}, \tag{16}$$

$$\mathbf{u} = \begin{pmatrix} \mathbf{E} \\ \mathbf{H} \end{pmatrix} \qquad \mathbf{q} = \begin{pmatrix} \mathbf{J} \\ \mathbf{M} \end{pmatrix}.$$

The Maxwell Operator $\Lambda_M(\beta)$ is defined on a dense subset of the Hilbert space U, given the parameter distribution β. When the conductivity is everywhere positive, $\sigma > 0$, (15) has a unique solution $\mathbf{u} \in U$ for each source $\mathbf{q} \in Y$, which we denote by

$$\mathbf{u} = [\Lambda_M(\beta)]^{-1}\,\mathbf{q}. \tag{17}$$

Given a solution $\mathbf{u}_j \in U$ of (15) corresponding to the source $\mathbf{q}_j \in Y$, we define the *measurements* $M_j\mathbf{u}_j$ by

$$M_j \quad : \quad U \quad \longrightarrow \quad Z_j \tag{18}$$

$$M_j\mathbf{u}_j(\mathbf{x}) := \left\{ \int_\Omega \delta(\mathbf{x} - d_{jk}) \begin{pmatrix} 0 & 0 \\ 0 & 1 \end{pmatrix} \begin{pmatrix} \mathbf{E}_j(\mathbf{x}) \\ \mathbf{H}_j(\mathbf{x}) \end{pmatrix} d\mathbf{x} \right\}_{k=1,\ldots,m_j}$$

with $\mathbf{u}_j = \begin{pmatrix} \mathbf{E}_j \\ \mathbf{H}_j \end{pmatrix}$, and with d_{jk}, $k = 1,\ldots,m_j$, being the detector positions corresponding to the source $\mathbf{q}_j$. The measurement operator M_j is well defined by (18) and maps the fields $\mathbf{u}_j \in U$ to a vector of complex numbers $M_j\mathbf{u}_j \in Z_j$, which consists of point measurements of the magnetic field components at the detector positions d_{jk}, $k = 1,\ldots,m_j$. More precisely, we can write

$$M_j \begin{pmatrix} \mathbf{E}_j \\ \mathbf{H}_j \end{pmatrix} = \left(\begin{pmatrix} 0 \\ \mathbf{H}_j(d_{j1}) \end{pmatrix}, \begin{pmatrix} 0 \\ \mathbf{H}_j(d_{j2}) \end{pmatrix}, \ldots, \begin{pmatrix} 0 \\ \mathbf{H}_j(d_{jm_j}) \end{pmatrix} \right)^T, \tag{19}$$

where the symbol ^{T} stands for transpose.

3.3 The residual operator

For each source $\mathbf{q}_j$, $j = 1,\ldots,p$, we define the *Forward Operator*

$$G_j \quad : \quad F \quad \longrightarrow \quad Z_j \tag{20}$$

$$G_j(\beta) := M_j\,\mathbf{u}_j,$$

where $\mathbf{u}_j$ is the solution of

$$\Lambda_M(\beta)\,\mathbf{u}_j = \mathbf{q}_j. \tag{21}$$

The operators G_j are *nonlinear* operators from the space of parameters F to the space of measurements Z_j.

Using the forward operators G_j, we formulate the inverse problem in the following way. Given the data

$$\hat{G}_j = \left(\begin{pmatrix} 0 \\ \hat{M}_{j1} \end{pmatrix}, \begin{pmatrix} 0 \\ \hat{M}_{j2} \end{pmatrix}, \ldots, \begin{pmatrix} 0 \\ \hat{M}_{jm_j} \end{pmatrix} \right)^T,$$

$$\hat{G}_j \in Z_j\,, \quad j = 1, \ldots, p, \tag{22}$$

find a parameter distribution $\tilde{\beta} \in F$ such that

$$G_j(\tilde{\beta}) \;=\; \hat{G}_j \tag{23}$$

is valid for all $j = 1, \ldots, p$. The *Residual Operators*

$$R_j \quad : \quad F \quad \longrightarrow \quad Z_j \tag{24}$$

are defined by

$$R_j(\beta) \;:=\; G_j(\beta) \;-\; \hat{G}_j,$$

so we can write (23) as

$$R_j(\tilde{\beta}) \;=\; 0 \qquad \text{for } j = 1, \ldots, p, \tag{25}$$

or in vector form

$$R(\tilde{\beta}) \;=\; 0, \tag{26}$$

with

$$R(\beta) \;:=\; (R_1(\beta)\,,\, \ldots\,,\, R_p(\beta))^T\,. \tag{27}$$

Equations (25) form a *system of nonlinear equations* for the unknown $\tilde{\beta}$. In the following we want to derive an efficient method for solving this system iteratively.

4 The adjoint field method

4.1 Linearization of the residual operator

For the derivation of the inversion algorithm that solves for $\tilde{\beta}$ in (26), we will need a suitable representation of the linearized residual R_j' of R_j. To find the form of R_j', we perturb β, $\mathbf{E}_j$ and $\mathbf{H}_j$ by

$$\beta \to \beta + \delta\beta \qquad \mathbf{E}_j \to \mathbf{E}_j + \mathbf{v}_j \qquad \mathbf{H}_j \to \mathbf{H}_j + \mathbf{w}_j, \tag{28}$$

and plug this into (8),(9). By neglecting terms of higher than linear order and applying the measurement operator M_j, we find that the linearized residual

$$R_j'(\beta) \quad : \quad F \quad \longrightarrow \quad Z_j$$

of R_j at β is given by

$$R_j'(\beta)\,\delta\beta \;=\; M_j \begin{pmatrix} \mathbf{v}_j \\ \mathbf{w}_j \end{pmatrix}, \tag{29}$$

where $\binom{\mathbf{v}_j}{\mathbf{w}_j}$ solves

$$\Lambda_M(\beta) \begin{pmatrix} \mathbf{v}_j \\ \mathbf{w}_j \end{pmatrix} \;=\; \begin{pmatrix} \delta\beta\,\mathbf{E}_j \\ 0 \end{pmatrix}. \tag{30}$$

We denote by $R'(\beta)$ the vector of linearized residuals for $R(\beta)$ in (27).

A typical Newton method for solving (26) is to start from a guess $\beta^{(0)}$ and to iteratively update β by writing

$$\beta^{(k+1)} = \beta^{(k)} + \delta\beta^{(k+1)} \tag{31}$$

where the update $\delta\beta^{(k+1)}$ solves the linearized residual equation

$$R'(\beta^{(k)})\,\delta\beta^{(k+1)} \;=\; -R(\beta^{(k)}) \tag{32}$$

This problem is ill-posed both in its continuum and discrete forms, and requires some form of regularization. A typical regularization amounts to solving (32) in a least squares sense with $\delta\beta$ restricted to have a fixed degree of regularity. In the next section we consider the direct least squares regularization of (32) when its discretized form is overdetermined, which is the case in our computations.

4.2 Least squares solution in the overdetermined case

The least squares solution of (32) is

$$\delta\beta = -[R'(\beta)^* R'(\beta)]^{-1} R'(\beta)^* R(\beta), \tag{33}$$

where $R'(\beta)^*$ is the adjoint of the linearized residual operator. In the discretized case $R'(\beta)$ is a matrix of size $m \times n$ where m is the number of (real) measurements and n is the number of pixels on which β is to be recovered. In one of our numerical experiments, described in section 6.3, we have 650 measurements for each of 18 source locations, so $m = 11700$. The number of pixels is $n = 20^3 = 8000$. Thus (32) is overdetermined (more data than unknowns) and the matrix $R'(\beta)^* R'(\beta)$ that we have to invert in (33) is 8000×8000. This matrix is ill-conditioned and requires regularization, which means that we have to invert $R'(\beta)^* R'(\beta) + \lambda I$ for a suitable λ. The main difficulty here is, however, the enormous computational cost of actually calculating this 8000×8000 matrix, for each step of the Newton iteration. It requires the solution of 8000 linearized residual problems each of which takes about 15 minutes in our computational setup.

In the next section we consider another way of approaching (32) which is much less computationally demanding and is what we implement in our numerical experiments.

4.3 The adjoint field method

Instead of solving (32) for all sources simultaneously, we try to solve it for one source at a time while updating the linearized residual operator after each determination of the incremental correction $\delta\beta$. So, in each step we only look for a solution of the equation

$$R_j'(\beta)\,\delta\beta_j \;=\; -R_j(\beta) \tag{34}$$

for a given index $j = 1, 2, \ldots, p$. After correcting β by

$$\beta \quad \longrightarrow \quad \beta + \delta\beta_j, \tag{35}$$

we use the updated residual equation (34) to compute the next correction $\delta\beta_{j+1}$. Doing this for one equation after the other, until each of the sources $\mathbf{q}_j$ has been considered exactly once, will yield one complete sweep of the Newton iteration. This procedure is similar to the Kaczmarz-method for solving linear systems, or the ART-method in x-ray tomography [20] and SIRT (Simultaneous Iterative Reconstruction Technique) as presented in [14]. We mention also that an analogous approach has been employed in ultrasound tomography by Natterer and Wübbeling [21], in more general bilinear inverse problems by Natterer [22], and in optical tomography by Dorn [16].

4.4 The minimization problem

In our numerical experiments the discretized form of (34) is for each j an underdetermined system, since $R_j^{'}(\beta)$ is a 650×8000 matrix. The minimal norm solution is

$$\text{Min } \|\delta\beta_j\|_2 \quad \text{subject to} \quad R_j^{'}(\beta)\delta\beta \; = \; -R_j(\beta), \tag{36}$$

and has the form

$$\delta\beta_j \; = \; -R_j^{'}(\beta)^*[R_j^{'}(\beta)R_j^{'}(\beta)^*]^{-1}R_j(\beta), \tag{37}$$

where $R_j^{'}(\beta)^*$ is as before the adjoint of $R_j^{'}(\beta)$.

We see from (37) that, in order to compute the correction $\delta\beta_j$, we have to first compute and then invert the matrix

$$C_j(\beta) \; := \; R_j^{'}(\beta)R_j^{'}(\beta)^*. \tag{38}$$

Since $R_j^{'}(\beta)$ changes with each update, we have to solve the linearized residual problem again for a very large number of times. This is still practically impossible to implement.

We can circumvent this difficulty by using an easy to compute (and invert) approximation of $C_j(\beta)$ in (37). This may be, for example, a diagonal matrix with positive elements, or some other positive definite matrix $\hat{C}_j$ with $\hat{C}_j \geq C_j(\beta)$. In this case the computed parameter distribution $\delta\beta_j$ will not solve equation (34). Our experience with optical tomography [16] and with the numerical experiments described in this paper indicates that, with suitable adjustments, we can achieve stable inversions. In cross-borehole tomography we have so far used a constant factor times the identity for $\hat{C}_j(\beta)$ and we have filtered out the output of the action of the adjoint operator near sources and receivers. We are considering at present several other possibilities for $\hat{C}_j(\beta)$, including coarse-graining of measurements to reduce computational complexity. We believe that the reason why these ad hoc replacements of $C_j(\beta)$ do produce stable and reliable results is that the inner iteration over the different sources tends to correct errors made by these replacements. There is no theoretical analysis to support these observations at present.

4.5 The adjoint of the linearized residual operator

Regardless of which of the above mentioned $C_j(\beta)$ we want to use, we need some efficient way to compute

$$R_j'(\beta)^*\zeta_j$$

for a given vector $\zeta_j \in Z_j$. We formulate the basic result here and derive it in Section 4.8 below.

Let

$$\zeta_j = \left(\begin{pmatrix} \eta_{j1} \\ \xi_{j1} \end{pmatrix}, \ldots, \begin{pmatrix} \eta_{jm_j} \\ \xi_{jm_j} \end{pmatrix} \right) \in Z_j. \tag{39}$$

Then $R_j'(\beta)^*\zeta_j \in F$ is given by

$$[R_j'(\beta)^*\zeta_j](\mathbf{x}) = \overline{\mathbf{E}_j(\mathbf{x})} \cdot \mathcal{E}_j(\mathbf{x}), \tag{40}$$

where $\mathbf{E}_j(\mathbf{x})$ is the solution of the direct problem

$$\Lambda_M(\beta) \begin{pmatrix} \mathbf{E}_j \\ \mathbf{H}_j \end{pmatrix} = \mathbf{q}_j, \tag{41}$$

and $\mathcal{E}_j(\mathbf{x})$ solves the corresponding adjoint problem

$$\Lambda_M^*(\beta) \begin{pmatrix} \mathcal{E}_j \\ \mathcal{H}_j \end{pmatrix} = \begin{pmatrix} 0 \\ \sum_{k=1}^{m_j} \xi_{jk}\delta(\mathbf{x} - d_{jk}) \end{pmatrix}, \tag{42}$$

with

$$\Lambda_M(\beta) = \begin{pmatrix} -\beta & \nabla\times \\ \nabla\times & \alpha \end{pmatrix} \quad , \quad \Lambda_M^*(\beta) = \begin{pmatrix} -\bar{\beta} & \nabla\times \\ \nabla\times & \bar{\alpha} \end{pmatrix}, \tag{43}$$

$$\begin{aligned} \beta &= i\omega\epsilon + \sigma, \qquad & \bar{\beta} &= -i\omega\epsilon + \sigma, \\ \alpha &= i\omega\mu, & \bar{\alpha} &= -i\omega\mu. \end{aligned} \tag{44}$$

4.6 Iterative algorithm for the adjoint field inversion

We will now describe in detail the algorithm which we use in the numerical experiments.

In brief algorithmic form, the iterative scheme can be written as

$\beta_p^{(0)} = \beta^{(0)}$

sweep_loop: DO $i = 1, I$

  $\beta_0^{(i)} = \beta_p^{(i-1)}$

  source_loop: DO $j = 1, p$

    $\delta\beta_j^{(i)} = -R_j'(\beta_{j-1}^{(i)})^*\hat{C}_j^{-1}R_j(\beta_{j-1}^{(i)})$

    $\beta_j^{(i)} = \beta_{j-1}^{(i)} + \tilde{\Gamma}_j\,\kappa_1\delta\beta_j^{(i)}$

  END DO source_loop

END DO sweep_loop

Here, $\beta^{(0)}$ is some initial guess for β and I is the total number of sweeps. The parameters κ_1, $\hat{C}_j$ and $\tilde{\Gamma}_j$ are chosen in order to improve the convergence and stability properties of the algorithm. In our numerical experiments $\beta^{(0)}$ is taken to be the correct layered background parameter distribution. The aim is to detect one or two inclusions which are imbedded in this layered background medium.

We have considerable freedom in choosing the location of the detectors corresponding to a given source position. In our numerical experiments we use 64 receiver locations at the surface of the earth, and 17 receivers in each of the boreholes except in the one which contains the active source.

For this distribution of receiver locations we assume that a useful first approximation $\hat{C}_j$ for the operator C_j is given by a constant $(\kappa_2)^{-1}$ times the identity operator. We multiply all residuals by the factor $\kappa_2 = 10^{10}$ before we apply the adjoint linearized residual operator. Using such a large value reduces the round-off error in the evaluation of the adjoint operator, since the order of magnitude of the residuals is very small (about 10^{-15}). Even after doing this, the output of the action of the adjoint operator still varies over several orders of magnitude. Near the sources and receivers it is quite large, whereas in the regions of interest, at some distance from sources and receivers, it is quite small. Therefore, to get a stable reconstruction scheme which is not too slow, we filter the output around the sources and receivers, and multiply the values in the interesting areas by a second factor κ_1. This factor changes in a progressive way, starting with 10^8, and increased by using the sweepnumber as a multiplicative factor. Since we are looking only for the isotropic conductivity distribution $\mathcal{R}e(\beta)$, we use only the real part of the computed update to correct the conductivity parameter. The imaginary part $\mathcal{I}m(\beta)$ does not change during the reconstruction process.

If the calculated update exceeds a given threshold value at a numerical cell, it is truncated and the threshold value is used instead as update. In addition, we apply minimal threshold values for the conductivity distribution. In our numerical experiments, we use half of the initial guess $\mathcal{R}e(\beta^{(0)})$ as minimum value in each cell. If the updated conductivity value is lower than this threshold, we use the threshold value instead. These threshold operators can be considered as applying an additional regularization to the updated conductivity distribution. In the algorithmic description given above, the filters around sources and receivers and the thresholds are combined in the operator $\tilde{\Gamma}_j$. Since $R_j'(\beta_{j-1}^{(i)})^*$ is linear, the factor κ_1 can also be thought of as part of the operator $\hat{C}_j$.

The filters which we apply around the source and receiver positions are chosen so that they are almost zero in the immediate vicinity of the source and receiver positions, and increase in a smooth way to 1 at some prescribed radius around these positions. These filters are multiplied with the computed updates. In our numerical calculations, the radius of the filters is about 3 grid cells (15m) around positions in the boreholes, and 9 grid cells (45m) around the surface detectors. This means that we practically do not update the first 45m below the surface. In the two numerical experiments that we present, we have found that without filtering numerical ghosts arise in these upper regions, which, however, do not prevent the correct detection of the inclusions situated in the deeper areas. An indication that the filtering helps comes from noting that if it is not used the discretized inverse problem is close to becoming underdetermined, even if we use all source positions. In this case the number of data is still $m = 11700$, but the number of unknowns increases to $n = 11200$.

In a practical scenario, this scheme could be modified so that different receiver groups are used to probe different subregions of Ω. The group of receivers used to probe a given subregion could be chosen according to the sensitivity [29] of these receivers to changes in the parameter distribution in the subregion of interest. We are currently investigating a method for calculating these sensitivities for given source-receiver locations in general media.

In one single step of the algorithm we have to solve one forward problem (41) to compute $R_j(\beta_{j-1}^{(i)})$, and one adjoint problem (42) to compute $\delta\beta_j^{(i)}$ out of $R_j(\beta_{j-1}^{(i)})$. We will describe the numerical implementation of these two steps in section 5.

4.7 Remarks on the adjoint field method

We collect several remarks about the adjoint field method used here, which are mostly of theoretical interest.

The electric field values in M_j of (19). The zeroes in the first component of the measurement vectors in (19) are there because we do not measure the electric components of the fields. They can be replaced by arbitrary complex numbers without changing the reconstruction process. If electric fields are measured then the operators M_j must be redefined by replacing the zero in the top left of the matrix in (18) by one.

The 'physical' measurement operator. The measurement operator defined by (18) is an idealization of the actual physical measurement process. It is not the values of the magnetic field at single points that are measured, but the integrals of these values over given detector surfaces. Using delta-like detectors simplifies the notation in the reconstruction method. However, in some situations it may be necessary to come back to a physically accurate model.

Uniqueness. Does the inverse problem have a unique solution in a certain class? In our applications, where we have to recover, in principle, the conductivity in the whole earth from a finite number of magnetic field measurements, the answer is negative. We do not have enough data. However, in related problems of medical imaging uniqueness results have been derived for certain cases. For more information about these (and related) results we refer to [10, 24, 26, 28, 30]. In medical imaging it can be assumed that, in principle, the whole Dirichlet-to-Neumann map on the boundary is known (see e.g. [28] for a definition of this map in the electromagnetic context). This gives enough information for the unique reconstruction of the conductivity distribution in the interior of a bounded domain from boundary data. This is definitely not true in geophysical applications, where we have access only to a small part of the boundary of the domain of interest.

Linearization and Fréchet-differentiability of R_j. The proof of linearizability or Fréchet-differentiability of R_j, and the choice of suitable function spaces, is not easy and will be part of future research. (See e.g. [15] for a proof in a similar situation arising in optical tomography.) We assume that the representation (29) of the linearized residual, or Fréchet-derivative, is essentially independent of the function spaces chosen. Note also that for proving Fréchet-differentiability of R_j it might be advantageous to take into account the finite extent of the measurement device, which in the present case is a wire loop. The data are then given by a surface integral of $\mathbf{H}(\mathbf{x})$ over the wire loop using Faraday's law. This has the advantage that trace theorems can be employed in the proof of the Fréchet-differentiability of the forward mapping.

4.8 Derivation of the adjoint operator in section 4.5

Let $\binom{\mathbf{v}}{\mathbf{w}}, \binom{\mathcal{E}}{\mathcal{H}} \in U$. Using Green's formulas for an infinite space, without boundary terms since $\sigma > 0$ everywhere, we have

$$\begin{aligned} \int_\Omega (\nabla \times \mathbf{w}) \cdot \bar{\mathcal{H}}\, d\mathbf{x} &= \int_\Omega \mathbf{w} \cdot \overline{(\nabla \times \mathcal{H})}\, d\mathbf{x}, \\ \int_\Omega (\nabla \times \mathbf{v}) \cdot \bar{\mathcal{E}}\, d\mathbf{x} &= \int_\Omega \mathbf{v} \cdot \overline{(\nabla \times \mathcal{E})}\, d\mathbf{x}, \end{aligned}$$

and so

$$\begin{aligned} &\left\langle \Lambda_M(\beta) \begin{pmatrix} \mathbf{v} \\ \mathbf{w} \end{pmatrix}, \begin{pmatrix} \mathcal{E} \\ \mathcal{H} \end{pmatrix} \right\rangle_{L^2} = \\ &\int_\Omega (\nabla \times \mathbf{w} - \beta \mathbf{v}) \cdot \bar{\mathcal{E}}\, d\mathbf{x} + \int_\Omega (\nabla \times \mathbf{v} + \alpha \mathbf{w}) \cdot \bar{\mathcal{H}}\, d\mathbf{x} \\ &= \int_\Omega \mathbf{v} \cdot \overline{(\nabla \times \mathcal{H} - \bar{\beta} \mathcal{E})}\, d\mathbf{x} + \int_\Omega \mathbf{w} \cdot \overline{(\nabla \times \mathbf{E} + \bar{\alpha} \mathcal{H})}\, d\mathbf{x} \\ &= \left\langle \begin{pmatrix} \mathbf{v} \\ \mathbf{w} \end{pmatrix}, \Lambda_M^*(\beta) \begin{pmatrix} \mathcal{E} \\ \mathcal{H} \end{pmatrix} \right\rangle_{L^2} \end{aligned} \tag{45}$$

with $\Lambda_M^*(\beta)$ defined in (43).

We will also use the identity

$$\int_\Omega \mathbf{w}(\mathbf{x}) \overline{\left[\sum_{k=1}^{m_j} \xi_{jk} \delta(\mathbf{x} - d_{jk}) \right]}\, d\mathbf{x} = \sum_{k=1}^{m_j} \left(\int_\Omega \mathbf{w}(\mathbf{x}) \delta(\mathbf{x} - d_{jk})\, d\mathbf{x} \right) \overline{\xi_{jk}}. \tag{46}$$

Combining (45),(46) yields

$$\begin{aligned} &\left\langle \Lambda_M(\beta) \begin{pmatrix} \mathbf{v} \\ \mathbf{w} \end{pmatrix}, \begin{pmatrix} \mathcal{E} \\ \mathcal{H} \end{pmatrix} \right\rangle_{L^2} + \int_\Omega \mathbf{w}(\mathbf{x}) \overline{\left[\sum_{k=1}^{m_j} \xi_{jk} \delta(\mathbf{x} - d_{jk}) \right]}\, d\mathbf{x} \\ &= \left\langle \begin{pmatrix} \mathbf{v} \\ \mathbf{w} \end{pmatrix}, \Lambda_M^*(\beta) \begin{pmatrix} \mathcal{E} \\ \mathcal{H} \end{pmatrix} \right\rangle_{L^2} + \sum_{k=1}^{m_j} \left(\int_\Omega \mathbf{w}(\mathbf{x}) \delta(\mathbf{x} - d_{jk})\, d\mathbf{x} \right) \overline{\xi_{jk}}. \end{aligned} \tag{47}$$

Now let $\binom{\mathbf{v}_j}{\mathbf{w}_j}$ be the solution of (30), $\binom{\mathbf{E}_j}{\mathbf{H}_j}$ the solution of (41), and $\binom{\mathcal{E}_j}{\mathcal{H}_j}$ the solution of (42). Then the second term on the left hand side of (47) and the first term on the right hand side of (47) cancel each other. The second term on the right hand side of (47) can be written as

$$\left\langle M_j \begin{pmatrix} \mathbf{v}_j \\ \mathbf{w}_j \end{pmatrix}, \zeta_j \right\rangle_{Z_j},$$

whereas the first term on the left hand side is equal to

$$\left\langle \begin{pmatrix} \delta\beta_j \mathbf{E}_j \\ 0 \end{pmatrix}, \begin{pmatrix} \mathcal{E}_j \\ \mathcal{H}_j \end{pmatrix} \right\rangle_{L^2} = \int_\Omega \delta\beta_j(\mathbf{x}) \mathbf{E}_j(\mathbf{x}) \cdot \overline{\mathcal{E}_j(\mathbf{x})}\, d\mathbf{x} = \left\langle \delta\beta_j, \overline{\mathbf{E}_j} \cdot \mathcal{E}_j \right\rangle_F.$$

Thus, (47) can be written as

$$\left\langle R_j'(\beta)\, \delta\beta_j, \zeta_j \right\rangle_{Z_j} = \left\langle \delta\beta_j, R_j'(\beta)^* \zeta_j \right\rangle_F$$

with $R_j'(\beta)^*\zeta_j$ defined by (40).

5 Discretization of Maxwell's equations

In order to implement the derived algorithm, we need a very efficient forward solver of the 3D system of Maxwell's equations in an infinite or semi-infinite domain. For this purpose, we have chosen to use and adapt the finite-difference frequency domain (FDFD) code which has been developed by Champagne *et al.* [9] for modeling the propagation of electromagnetic radiation in conductive materials. We will outline here only the main features of the code, and refer for more details to [9] and to more complete descriptions of the code that are currently in preparation.

5.1 The finite-difference, frequency domain formulation

The implementation given in [9] can be considered as an extension to lossy media of a finite-difference frequency-domain formulation that was developed earlier by Beilenhoff *et al.* [3] for boundary scattering in lossless media. Since we have to model an infinite medium using a finite-dimensional computational domain, we use in addition an anisotropic PML (perfectly matched layer) in order to avoid reflections at the artificial computational boundaries. Here we follow mainly the work of Berenger [4] and Sacks *et al.* [27]. The absorbing regions have material parameters similar to those proposed by Kuzuoglu *et al.* [19]. The code is designed to be able to model media with general anisotropic parameter distributions $\beta(\mathbf{x})$ and $\alpha(\mathbf{x})$ in the domain Ω. This feature of the code has not yet been utilized here since the models were assumed to be locally isotropic. However, it will become important in future research when we consider the problem of recovering more general anisotropic conductivity distributions from field data by a generalization of the new reconstruction scheme. Anisotropy is expected to become important, for example, when model cells contain oriented fractures filled with conducting fluid.

The derivation of the FDFD formulation starts from an integral representation of Maxwell's curl equations (Ampère's and Faraday's laws) (1),(2):

$$\oint_{\mathcal{C}} \mathbf{H} \cdot dl \,=\, i\omega \int_{\mathcal{S}} (\overline{\epsilon} \cdot \mathbf{E}) \cdot \hat{\mathbf{n}} \, dS \,+\, \int_{\mathcal{S}} \mathbf{J} \cdot \hat{\mathbf{n}} \, dS \tag{48}$$

and

$$\oint_{\mathcal{C}} \mathbf{E} \cdot dl \,=\, -i\omega \int_{\mathcal{S}} (\overline{\mu} \cdot \mathbf{H}) \cdot \hat{\mathbf{n}} \, dS \,+\, \int_{\mathcal{S}} \mathbf{M} \cdot \hat{\mathbf{n}} \, dS, \tag{49}$$

where $\mathcal{C}$ is the boundary of the open surface S. The parameters $\overline{\epsilon}$ and $\overline{\mu}$ (where the bars over the symbols indicate in this paragraph always a result of some averaging procedure rather than 'complex conjugate') are now diagonal dyads with complex numbers on the main diagonal. In the isotropic case (which is all we consider in this paper), they are related to the parameters α and β inside the domain Ω by

$$\overline{\mu}(\mathbf{x}) \,=\, (i\omega)^{-1}\mathbf{diag}(\overline{\alpha}(\mathbf{x}), \overline{\alpha}(\mathbf{x}), \overline{\alpha}(\mathbf{x})) \quad , \quad \overline{\epsilon}(\mathbf{x}) \,=\, (i\omega)^{-1}\mathbf{diag}(\overline{\beta}(\mathbf{x}), \overline{\beta}(\mathbf{x}), \overline{\beta}(\mathbf{x})),$$

where $\overline{\alpha}(\mathbf{x})$ and $\overline{\beta}(\mathbf{x})$ are values of $\alpha(\mathbf{x})$ and $\beta(\mathbf{x})$ averaged over a small neighborhood of the given point $\mathbf{x} \in \Omega$ (see the further discussion in the sequel). In the surrounding PML material, however, the three components of the diagonal dyads $\overline{\alpha}(\mathbf{x})$ and $\overline{\beta}(\mathbf{x})$ in a given point differ from each other. In these regions, the parameters are chosen carefully to achieve the desired properties of the absorbing PML region, namely being nonreflecting for radiation leaving the interior of the computational domain. We provide more details about the implementation of the PML in the following subsection.

The computational domain is discretized into small boxes (elementary cells) using a staggered grid (see Figure 2). All material parameters are assumed constant in a given elementary cell. The electric field values and the values of the material parameter β are attached to the central points of the edges of these boxes, whereas all magnetic field values and the values of the material parameter α are attached to the central points of the surfaces of the elementary cells. The average material parameters $\overline{\alpha}(\mathbf{x})$ and $\overline{\beta}(\mathbf{x})$ in those points are obtained by averaging over α and β in the cells adjacent to the grid point under consideration. After having discretized the computational domain Ω in this way, the integrals in (48) and (49) can be approximated by putting

$$\int_{-a/2}^{a/2} \mathbf{f} \cdot d\mathbf{l} \approx a f_m \quad , \quad \int_{-a/2}^{a/2} \int_{-b/2}^{b/2} \mathbf{g} \cdot \hat{\mathbf{n}} \, dS \approx ab g_m. \tag{50}$$

In (50) a,b are the lengths of the edges surrounding the rectangular surface of integration, f_m is the value of the field $\mathbf{f}$ at the center of the edge under consideration, and g_n is the value of the field $\mathbf{g}$ at the center of the corresponding surface.

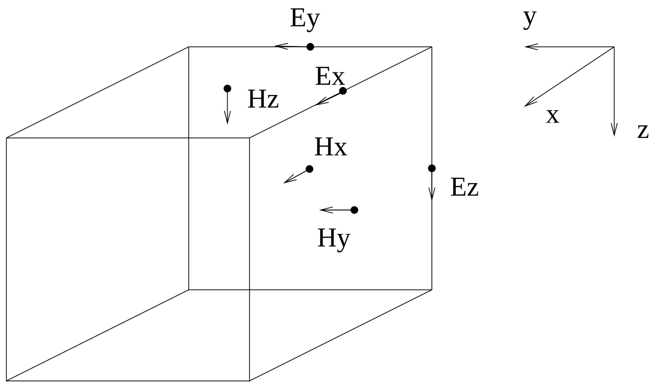

Figure 2: One box of the staggered grid. The electric field values and the values of the material parameter β are attached to the central points of the edges of these boxes, whereas all magnetic field values and the values of the material parameter α are attached to the central points of the surfaces of the elementary cells.

It follows from (48) and (49) that the values g_m are essentially products of the (electric or magnetic) fields at the center point of an integration surface and the value of the corresponding material parameters at this point. Analogously, the values f_m are products of the (electric or magnetic) fields at the center points of the edges surrounding the integration surface and the corresponding material parameters at those points.

In this way the discretized versions of Ampère's law and Faraday's law may be derived for all possible surfaces of the staggered grid and this procedure yields a system of equations for the electric and magnetic field values at the grid points (see [9]). Following standard practice, either the magnetic or the electric field can be eliminated from this system. In our implementation, we have chosen to eliminate the magnetic field values h, and to solve for the (vector of discretized) electric field values e. The resulting system has the form

$$\mathbf{A}^T \mathbf{D}_{\bar{l}} \mathbf{D}_{\mu}^{-1} \mathbf{D}_A^{-1} \mathbf{A} \mathbf{D}_l \, e \; - \; k_0^2 \mathbf{D}_\epsilon \, e \; = \; -i\omega\mu_0 \mathbf{D}_{\bar{A}} \, j \; - \; \mathbf{A}^T \mathbf{D}_{\bar{l}} \mathbf{D}_{\mu}^{-1} \, m. \tag{51}$$

Here, e, j and m denote the (vectors of the discretized) electric field, the electric source currents, and the magnetic source currents, respectively. The symbols $\mathbf{D}_\epsilon$ and $\mathbf{D}_\mu$ denote diagonal matrices that contain the material parameters $\bar{\epsilon}$ and $\bar{\mu}$, and the symbols $\mathbf{D}_{\bar{l}}$, $\mathbf{D}_A$, $\mathbf{D}_l$, and $\mathbf{D}_{\bar{A}}$ denote diagonal matrices that contain information about the geometry of the grid. The matrix $\mathbf{A}$ models essentially the line integrals of (48) and (49).

Note: The system (51) can be considered to be a discretized version of the vector Helmholtz equation

$$\nabla \times (\bar{\mu}_r^{-1} \cdot \nabla \times \mathbf{E}) \; - \; k_0^2 \bar{\epsilon}_r \cdot \mathbf{E} \; = \; -i\omega\mu_0 \mathbf{J} \; - \; \nabla \times \bar{\mu}_r^{-1} \cdot \mathbf{M}, \tag{52}$$

which is commonly used in finite element codes.

A commonly observed problem in numerical computations of Maxwell's equations arises due to a possible resonance at zero frequency, which might cause the resulting system matrix to have an eigenvalue at zero and therefore not being positive definite or invertible. For the geometries considered here, the fields for resonant frequency of 0 Hz are generated only by electric charges within the volume. Such charges may develop as an artifact of numerical roundoff when evaluating the vector wave equation, especially at lower frequencies. To avoid this problem, we eliminate any charge within the volume by incorporating in the numerical scheme a term analogous to

$$\nabla[\nabla \cdot (\bar{\epsilon}_r \cdot \mathbf{E})] \;=\; \mathbf{0}, \tag{53}$$

which corresponds to enforcing satisfaction of equation (3) (Gauss' Law). Discretizing (53), and adding the result to (51), yields (after some additional symmetrization) a system for the calculation of the electric field vector e out of the given sources j and m. This system can be solved iteratively, for example, using the Bi-CGSTAB scheme of van der Vorst [31]. For more details we again refer to [9] and to the discussion in the next subsection.

5.2 The PML formulation for mesh truncation

The computational mesh is truncated using perfectly matched layers (PML) that absorb electromagnetic waves following the general ideas of Berenger [4]. The PML is a representation of anisotropic media that satisfy

$$\mathbf{D} \;=\; \bar{\epsilon}_{\mathrm{PML}} \cdot \mathbf{E} \quad \text{and} \quad \mathbf{B} \;=\; \bar{\mu}_{\mathrm{PML}} \cdot \mathbf{H}, \tag{54}$$

where

$$\bar{\epsilon}_{\mathrm{PML}} \;=\; \bar{\epsilon} \cdot \mathbf{\Lambda} \quad \text{and} \quad \bar{\mu}_{\mathrm{PML}} \;=\; \bar{\mu} \cdot \mathbf{\Lambda}, \tag{55}$$

with $\mathbf{D}$ and $\mathbf{B}$ denoting the electric displacement and the magnetic induction, respectively. The symbol $\mathbf{\Lambda}$ stands for a diagonal dyad that has entries selected to absorb incident electromagnetic waves. The form of this dyadic quantity is determined by the normal to the PML interface. As an example, for a PML interface with a normal in the z direction, the form of $\mathbf{\Lambda}$ is given by Kuzuoglu and Mittra [19] and by Wu *et al.* [36] as

$$\mathbf{\Lambda}_z \;=\; \begin{bmatrix} a & 0 & 0 \\ 0 & a & 0 \\ 0 & 0 & 1/a \end{bmatrix}, \tag{56}$$

in which a is given by

$$a \;=\; 1 \;+\; \frac{f(x,y,z)}{1 + i\gamma_1 \omega}. \tag{57}$$

Here, γ_1 is a constant and $f(x, y, z)$ is a function of position that falls to zero at the interface between the modeling space and the desired PML boundary. In the present implementation, we use

$$a = 1 + \frac{(1-i)\gamma_2}{\rho(x,y,z)(1+i\epsilon_0\omega)}, \tag{58}$$

where $\rho(x, y, z)$ is a discretized distance from the modeling space/PML interface to the centroid of the cell of interest in the PML. γ_2 is chosen to determine the amplitude of $f(x, y, z)$. This particular choice was found empirically by Champagne *et al.* [9] to give satisfactory results for the present problem. The search for optimal choices of the function $f(x, y, z)$ continues.

6 Numerical experiments

The numerical experiments which we have performed so far to test the new algorithm, are based on the Lost Hills model which is described by Buettner [8]. The physical experiments of [8] have been done at Mobil Oil's Lost Hills-3 field in San Joaquin Valley, which is an interesting test site for our purposes since it can be viewed as an excellent analog of a shallow environmental remediation using steam injection. Earlier work at this test site has been done by Wilt *et al.* [35]. This means that real data are available for these sites, which can be used in future work to test the behavior of the algorithm in a realistic scenario. In our numerical experiments up to now, however, we do not use these data, but create instead synthetic data by running the forward code on the correct model. In addition, in order to test different situations, we choose the number and locations of the boreholes, sources and receivers independently from the physical experiments which are described in [8].

6.1 The Lost Hills model

The Lost Hills model in our numerical experiments consists of a layered background medium in which one or two 3D-inclusions are imbedded. There are six layers in total, of which the uppermost contains the air, and the remaining five layers contain soil and rock materials. The total size of the domain is (in XYZ-direction) 120mx160mx185m. The layers have, starting with the air and going downwards, extensions in Z-direction (in short 'Z-extension') of, respectively, 40m (0.0 Siemens/m), 30m (0.3 S/m), 30m (0.15 S/m), 20m (0.06 S/m) (contains inclusions), 30m (0.06 S/m), and 30m (0.2 S/m), where the numbers in parentheses give the conductivity values inside these layers. Inclusions (for example injected plumes of conducting steam) are located in the layer with a depth ranging from 60m to 80m below the free surface. The Z-extension of these plumes are, for simplicity, chosen to be the same as the Z-extension of the layer in which they are imbedded (20m). It is assumed that the injected steam has a conductivity of 0.2 S/m. The relative permittivity and relative permeability is chosen to be 1.0 everywhere in all of our numerical examples. Two different views of the model (from the top and from the front) are given in Figures 3,4,5, and 6. These figures also show the shapes of the inclusions (injected steam zones) which we want to recover in our two numerical experiments.

In a typical physical experiment of cross-borehole or surface to borehole electromagnetic imaging, gathered data usually consists of the amplitude and the phase of the radial and vertical components of the magnetic field (see for example [8]). In our numerical experiments, we assume that we measure all three cartesian components of the magnetic field (real and imaginary part) at the detector locations. If not all three components are available from a physical experiment, the measurement operator in (18),(19) has to be adjusted accordingly.

In addition, we assume at present that there is no noise in the measured data. Using the same forward code for creating the data as for the reconstruction process is commonly known as 'inverse crime'. From the comparison of real data with data created by the FDFD code for an approximate model of the Lost Hills experiment (see Champagne [9]), and from comparison with an analytical solution, we are confident that the general behavior of the algorithm will not change when adding noise to the synthetically created data, or when using real data for the reconstruction task. This has, however, not yet been tested.

6.2 Discretization of the Lost Hills model

We discretize the Lost Hills model described above by using a 20x20x37 staggered grid for the physical domain, which is surrounded by 10 cells of PML on each side. Each of the individual grid cells in the physical domain has a size of 6mx8mx5m. Therefore, the total physical domain which is modelled by the computational grid has size 120mx160mx185m. The physical domain is surrounded by a region of PML, 10 cells thick. Each of the cells in this region has an extension of 10m in the direction away from the physical domain. The total grid which is used in our computations is therefore 40x40x57 and has a total size of 320mx360mx385m (including the artificial PML). Different cross-sections through this grid are shown in the figures 7,8,17,18. These figures show the correct physical size of the grid including the PML. Chosen as reference position for each cell is in all figures the position of the x-component of the electric field (or conductivity) in the staggered grid (see Figure 2).

The sources used are in all examples z-directed magnetic dipole sources of the strength $1\mathrm{Am}^2$ and with frequency $f = 1.022$kHz. They are located in the boreholes (indicated in the figures 7,17 by 'O'). The PML layer is characterized by (58) with $\gamma_2 = 1$. Our experience from the computational examples is that with this value is reflections at the artificial boundaries are avoided.

We use the Bi-CGSTAB scheme of van der Vorst [31] for the solution of the discretized Maxwell system which was derived in section 5.1. We perform 100 iterations of the Bi-CGSTAB scheme for each forward and adjoint problem. This yields a tolerance in the solution of about 10^{-5}. In our numerical experiments Bi-CGSTAB scheme performs stably for the level of accuracy imposed. The calculation of one forward problem and one adjoint problem for a given source position needs altogether about 15 minutes on a DEC ALPHA 8400 or on an SGI Octane. All computations are serial and require 140MB of memory for the 40x40x57 example described above.

6.3 Numerical experiment recovering one large inclusion

The setup of our first numerical experiment is described in figures 3 and 4. An inclusion of physical size 24mx96mx20m or 4x12x4 grid cells (cells are not cubes, see subsection 6.2) is imbedded in the layer of the Lost Hills model ranging from the depth of 60m to 80m. The conductivity in the inclusion is 0.2 S/m, and the conductivity in the background layer is 0.06 S/m. All remaining parameters (electric permittivity and magnetic permeability) are constant in the whole domain. Three boreholes are arranged so that the inclusion is located between them. In each of the boreholes, six equally spaced z-directed (vertical) dipole transmitters are located at depths of 10m, 30m, 50m, 70m, 90m, 110m below the free surface, of which only one is active at a time. In each borehole, 22 receivers are positioned equally spaced from the free surface down to a depth of 110m. At the surface of the earth, 64 receivers are equally spaced. The magnetic field at the receiver positions is measured, and the aim is to recover the conductivity of the inclusions given the recorded data. As initial guess for our iterations, we use the correct layered background material.

We apply filters of radius 15m around the sources and receivers in the boreholes of and of radius 45m around the surface detectors. Therefore, the region directly below the free surface is usually not updated. Here we use our knowledge that the plumes are injected at a given depth. If these near-surface regions have to be recovered, too, then we have to adapt our strategy by either updating the whole domain at the same time, or by starting with the data near the free surface first to reconstruct the upper regions, and then marching downward by using more and more of the data corresponding to the detectors and sources which are located in the deeper region. Both strategies probably require more data than we use in our reconstructions at present, which is indicated by the following count of data and unknowns.

The region which has to be reconstructed has about 20x20x20 grid cells. These are $20^3 = 8000$ unknown real numbers, the conductivities at these grid cells. Here we have taken into account that the conductivity in the near-surface region is practically unchanged during the reconstruction process because of the filtering of the updates. For each of the source positions we have 650 real numbers given as data (three complex components of the magnetic field at each detector, but not at the detectors situated in the same borehole as the active source). For 18 sources there are a total of 11700 real numbers as data. Therefore, in the discretized setting, our inverse problem is slightly overdetermined. If we include the near-surface region in our calculation, then we have to recover about 20x20x30 grid cells or 12000 real numbers (instead of 8000) from the given data, which is a little harder to achieve.

Figures 7 to 16 show the original objects and some results of the reconstruction process after running one sweep and twenty sweeps of the adjoint field method

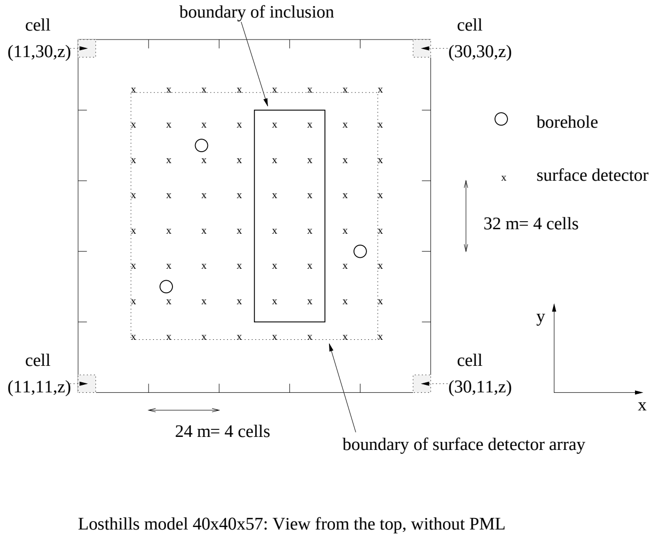

Figure 3: The figure shows the setup used in the first numerical experiment (without the PML). The view is from the top of the earth. A large inclusion (injected steam zone) is situated at a depth ranging from 60m to 80m below the surface, and is surrounded by three boreholes. 64 receivers (indicated in the figure by 'x') are equally spaced at the surface.

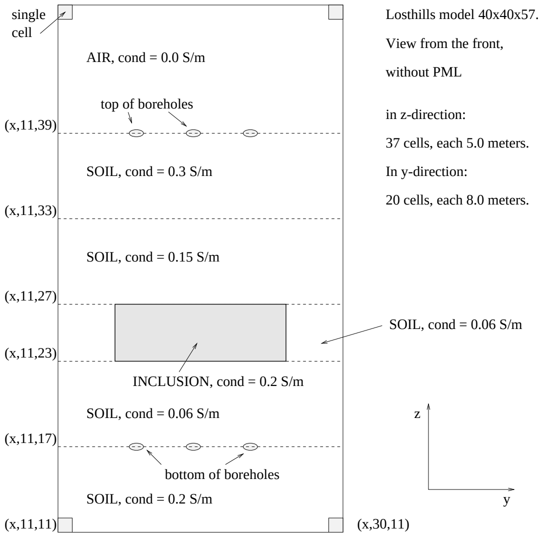

Figure 4: The figure shows the setup used in the first numerical experiment (without the PML). It is a vertical cross-section through the domain. The top layer contains the air and the remaining layers contain soil and rock materials. The inclusion is imbedded in a background layer with a conductivity of 0.06 S/m and has a conductivity of 0.2 S/m. Three boreholes are positioned around the inclusion which are also shown in Figure 3. The top and bottom parts of the boreholes are indicated in the figure. Each of these boreholes contains six equally spaced z-directed dipole transmitters at depths of 10m,30m,50m,70m,90m,110m below the free surface, with only one active at a time. In each borehole, 22 receivers are arranged equally spaced from the free surface down to a depth of 110m and the inclusion is located at a depth ranging from 60m to 80m.

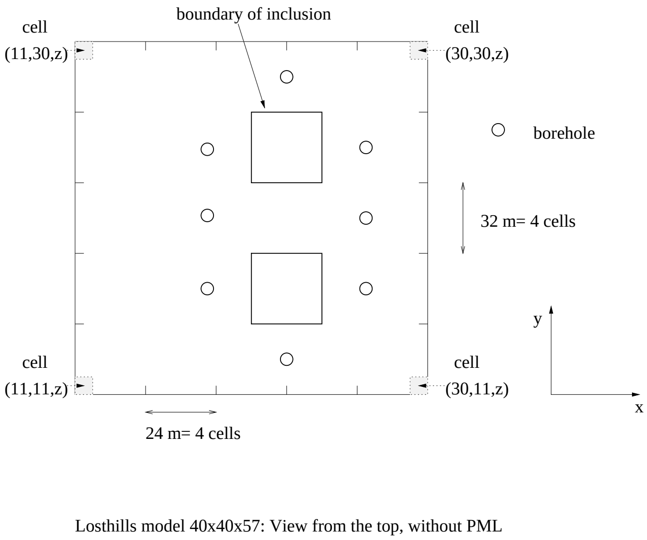

Figure 5: The figure shows the setup used in the second numerical experiment (without the PML). The view is from the top. Two small inclusions (injected steam zones) are situated at a depth ranging from 60m to 80m below the surface, and are surrounded by eight boreholes. 64 receivers (indicated in Figure 3 by ‘x’) are equally spaced at the surface.

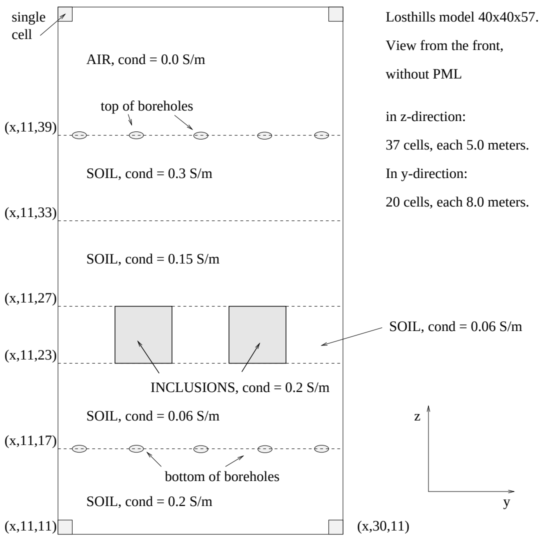

Figure 6: The figure shows the setup used in the second numerical experiment (without the PML). It is a vertical cross-section through the domain. The top layer contains the air, and the remaining layers contain soil and rock materials. The two inclusions are imbedded in a background layer with a conductivity of 0.06 S/m and have conductivities of 0.2 S/m. Eight boreholes are positioned around the inclusion which are also displayed in Figure 5. The top and bottom parts of the boreholes are indicated in the figure. Each of these boreholes contains three equally spaced z-directed dipole transmitters at depths of 35m,70m,105m below the free surface, of which only one is active at a time. 17 receivers are arranged equally spaced in each borehole, starting at a depth of 30m and going down up to 110m. The two inclusions are located at a depth ranging from 60m to 80m.

starting from the initial guess. We restrict the graphical display of the results to two cross-sections of the domain, both containing the correct location of the inclusion. One is a horizontal cross-section (which we call 'view from the top') at a depth of 70m below the free surface, and the other one is a vertical cross-section (which we call 'view from the front') with constant x-coordinate lying at the center of the correct inclusion. We will keep this scheme also for the display of the results of the second example.

We note that the cross-sections shown are representative of the reconstructions in the sense that we did not observe significant features or artifacts in the remaining parts of the physical domain during the reconstruction process which are not visible also on the cross-sections shown.

In the following we will discuss Figures 7 to 16 one by one. Note that figures with odd numbers (7,9,...,15) refer always to horizontal cross-sections ('view from the top'), whereas figures with even numbers (8,10,...,16) refer to vertical cross-sections ('view from the front').

6.3.1 The true conductivity model

The left side of Figure 7 shows the true conductivity distribution of the Lost Hills model with one large inclusion. The view of the figure is from the surface of the earth, and the cross-section is positioned 70m below the free surface. The aim in the reconstruction process will be to recover the indicated inclusion out of the given data. The three boreholes are indicated by an 'O', and the edges of the inclusion are indicated by an 'X'. The inner part of the mesh with smaller grid cells models the physical domain of interest, whereas the outer part models the PML. On the right hand side of Figure 7 is a plot of the conductivity distribution along the line shown in the figure. The conductivity of the inclusion is 0.2 S/m, imbedded in a background medium with conductivity 0.06 S/m. The outer slopes in the plot correspond to the PML.

Next, for comparison with Figure 7, Figure 8 shows the same Lost Hills model as that in Figure 7. On the left is now displayed the true conductivity distribution of a vertical cross-section of the earth with constant X-values, which goes through the center of the inclusion. The inner part of the mesh contains the domain of physical interest, and the outer part contains the PML. The part of the mesh colored in dark blue indicates the layer containing air and the adjacent PML. The layers beneath this dark blue region contain soil and rock materials with varying conductivity values (between 0.06 S/m and 0.3 S/m.) The edges of the true inclusion are indicated by an 'X'. On the right hand side of Figure 8, the plot shows the variation of the conductivity over the vertical cross-section indicated in the figure on the left. The sharp edges of the original Lost Hills model are smoothed out slightly by the discretization scheme when averaging the parameters over adjacent cells.

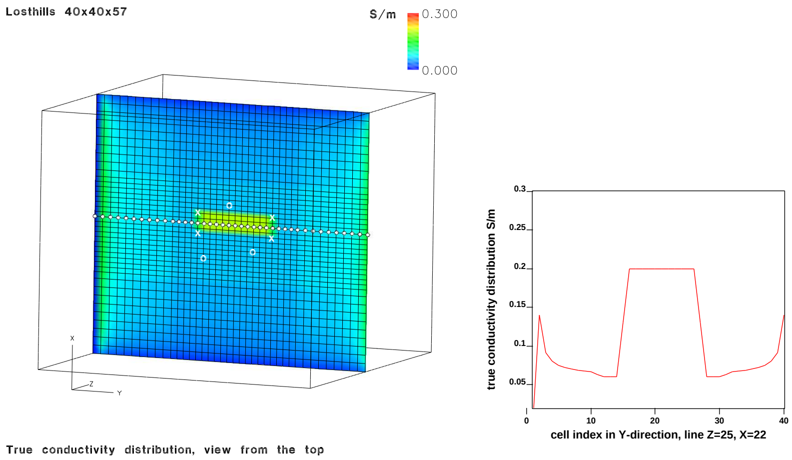

Figure 7: *Left.* This figure shows the true conductivity of the Lost Hills model with one large inclusion (including the PML). The view is from the surface. The three boreholes are indicated by an 'O', and the edges of the inclusion are indicated by an 'X'. *Right:* Plot of the conductivity along the line shown on the left.

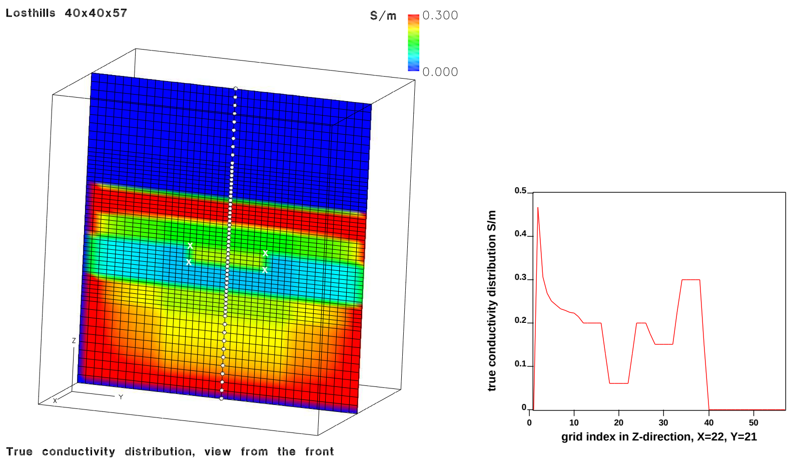

Figure 8: *Left:* The same Lost Hills model is shown as in Figure 7. Now the true conductivity is shown on a vertical cross-section of the earth with constant x-values, which goes through the center of the inclusion. The edges of the true inclusion are indicated by an 'X'. *Right:* Plot along the vertical cross-section indicated in the figure.

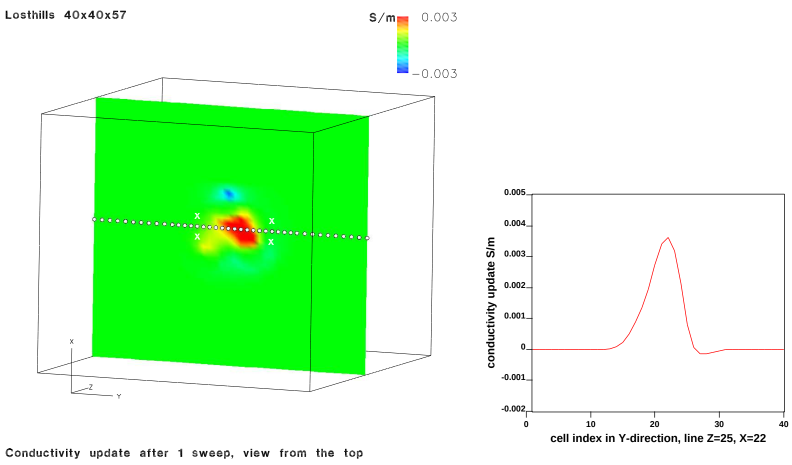

Figure 9: *Left:* The accumulated update of the conductivity after one sweep of the algorithm, on the same plane as in Figure 7. The view is from the top. The edges of the inclusion are indicated by an ‘X’. *Right:* Cross-section along the line indicated on the left.

6.3.2 One-sweep reconstruction

In Figure 9 on the left we show the accumulated update of the conductivity distribution after one sweep of the algorithm in the same plane as displayed in Figure 7. The view is from the top. The figure can alternatively be described as showing the difference between the reconstruction of the conductivity after one sweep, and its initial guess. The initial guess in the presented reconstructions is the correct layered background conductivity distribution. The edges of the inclusion which has to be identified are indicated by an ‘X’. Displayed in Figure 9 on the right is the cross-section along the line indicated in the left figure. The accumulated conductivity update after one sweep is still quite small, since we multiply the updates of the conductivity during the early sweeps of the algorithm with a scaling factor, which is increased progressively during the succeeding sweeps.

Again, for direct comparison with Figure 9, the left hand side of Figure 10 shows that the accumulated update of the conductivity after one sweep. Shown is the same vertical cross-section (with constant coordinate X=22) as in Figure 8. The Z-axis in the figure points out of the earth into the air. The edges of the inclusion are indicated by an ‘X’. The right side of Figure 10 is the accumulated conductivity update on the line indicated in the figure. After one sweep, the accumulated update is still small.

The reconstructed conductivity is shown in Figure 11 on the left, after one sweep. The view is from the top. This figure shows the sum of the initial conductivity guess

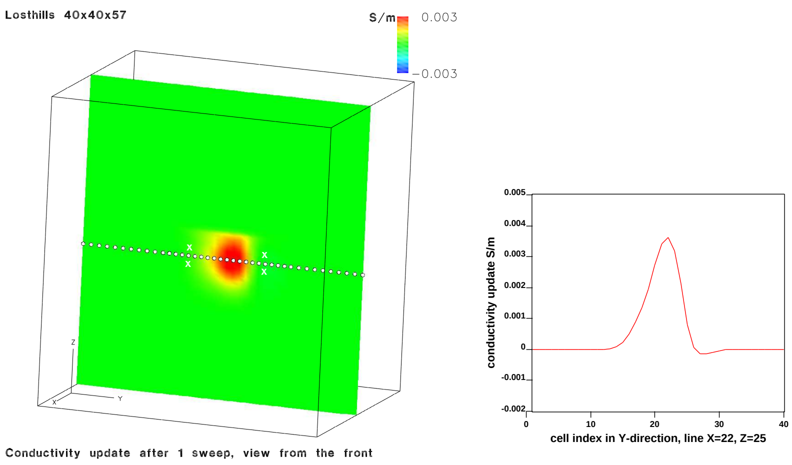

Figure 10: *Left:* Accumulated update of the conductivity after one sweep on the same vertical cross-section (with constant coordinate X=22) as in Figure 8. The edges of the inclusion are indicated by an 'X'. *Right:* Plot of the accumulated conductivity update along the line indicated in the figure. After one sweep, the accumulated update is still small.

and the accumulated update of Figure 9 on the same cross-section. The initial guess is the correct layered background conductivity, including the PML. The conductivity inside the PML is not updated during the reconstruction. The edges of the inclusion are indicated by an 'X'. The right hand plot is along the line indicated in the figure on the left. After one sweep of the algorithm, the contrast between the conductivity of the detected inclusion and the background is still small.

The left side of Figure 12 shows the reconstructed conductivity after one sweep, on the same vertical cross-section with constant X-coordinate (X=22) as in Figures 8, 10, 14. The figure shows the sum of the conductivity used as initial guess (the layered background medium) and the accumulated update shown in Figure 10. However, the coloring scheme is different here. The contrast of the detected inclusion is still very small compared to the contrast between the conductivity of the different layers, so that it is not easily observable in this display. The right side of Figure 12 is a plot along the line indicated in the left hand figure. The magnitude of the detected object after one sweep is still small.

6.3.3 Twenty-sweep reconstruction

On the left, Figure 13 shows the same cross-section of the accumulated update as Figure 9, but after 20 sweeps of the adjoint field algorithm. The shape of the reconstructed inclusion is now closer to the shape of the true inclusion, which is indicated

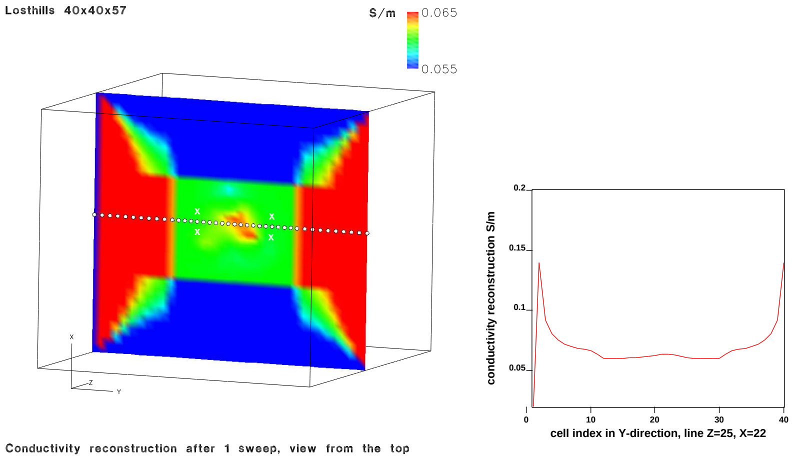

Figure 11: *Left:* Reconstructed conductivity after one sweep. View from the top. This figure shows the sum of the initial conductivity guess and the accumulated update of Figure 9 in the same cross-section. *Right:* Plot along the line shown on the left. After one sweep the contrast between the conductivity of the detected inclusion and the background is still small.

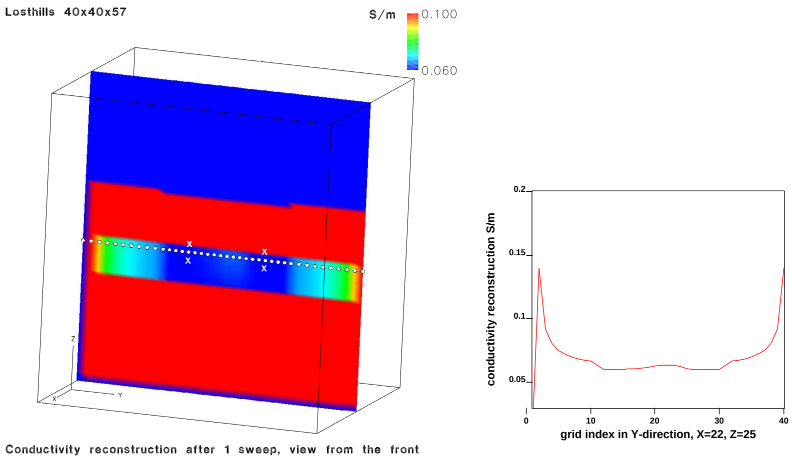

Figure 12: *Left:* Reconstructed conductivity after one sweep shown on the same vertical cross-section with constant X-coordinate (X=22) as in Figures 8,10,14. The contrast of the detected object is still very small compared to the contrast between the conductivity of the different layers, so that it is not easily observable. *Right:* Plot along the line shown on the left.

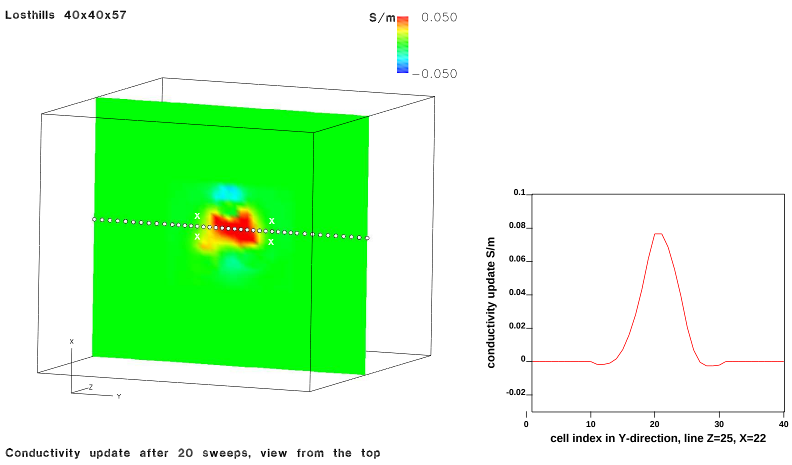

Figure 13: *Left:* The figure shows the accumulated update of the conductivity on the same cross-section as Figure 9, but after 20 sweeps of the adjoint field algorithm. The shape of the reconstructed inclusion is now closer to the shape of the true inclusion, which is indicated by an 'X'. *Right:* The accumulated conductivity update along the line indicated in the figure.

by an 'X'. Comparison with Figure 7 shows that the part of the inclusion which is located inside the triangle defined by the three borehole locations, is recovered best. Clearly visible are also the negative updates outside this triangle, which presumably are caused by the dipole character of the elementary updates. The right side of Figure 13 shows the accumulated conductivity update along the line indicated in the figure. The peak value on this line is 0.08 S/m. This is already close to the true contrast value of 0.14 S/m.

The accumulated update of the conductivity shown on the left of Figure 14 is on the same vertical cross-section as in Figure 10, but after 20 sweeps. The edges of the true inclusion are indicated by 'X'. The shape of the reconstructed inclusion is now much closer to the correct one. The part of the inclusion which is covered by the area of the triangle defined by the three borehole positions, is reconstructed best. Note the phantom in the reconstruction which appears between the reconstructed inclusion and the free surface. It is presumably caused by the large number of surface detectors. The right hand side of Figure 14 shows the accumulated update along the line shown in the figure. The peak value (0.08 S/m) is close to the true conductivity difference between the inclusion and the background layer (0.14 S/m).

On the left Figure 15 is the reconstructed conductivity on the same cross-section as in Figure 11, but after 20 sweeps. The conductivity shown is the sum of the

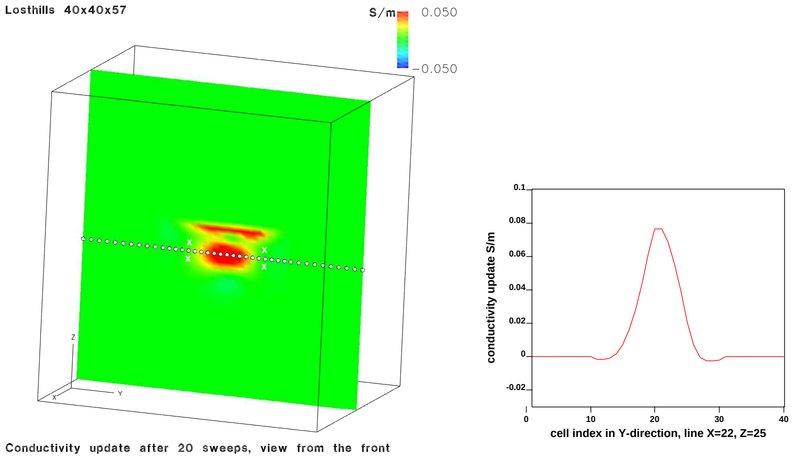

Figure 14: *Left:* The accumulated update of the conductivity on the same vertical cross-section as in Figure 10, but after 20 sweeps. The edges of the true inclusion are indicated by 'X'. The shape of the reconstructed inclusion is now much closer to the correct one. *Right:* Plot of the accumulated update along the line shown in the figure.

conductivity distribution of the layered background medium and the accumulated update after 20 sweeps shown in Figure 13. The shape of the detected inclusion is now much closer to that of the true inclusion (indicated by the 'X'). Note that the coloring scheme is different from that used in Figure 11. On the right of Figure 15 is the cross-section along the line which is indicated on the left. The peak value of this plot (0.14 S/m) is already close to the conductivity in the true inclusion (0.2 S/m).

On the left Figure 16 is the reconstructed conductivity on the same cross-section as in Figure 12, but after 20 sweeps of the adjoint field algorithm. The coloring scheme has not been changed in order to compare with Figure 12. The inclusion is now more visible than after only one sweep. The edges of the true inclusion are indicated by an 'X'. On the right of Figure 16 is the plot along the line on the left. This plot has the same scale as the one shown in Figure 12. The improvement in the reconstruction between the first and the twentieth sweep is clearly visible.

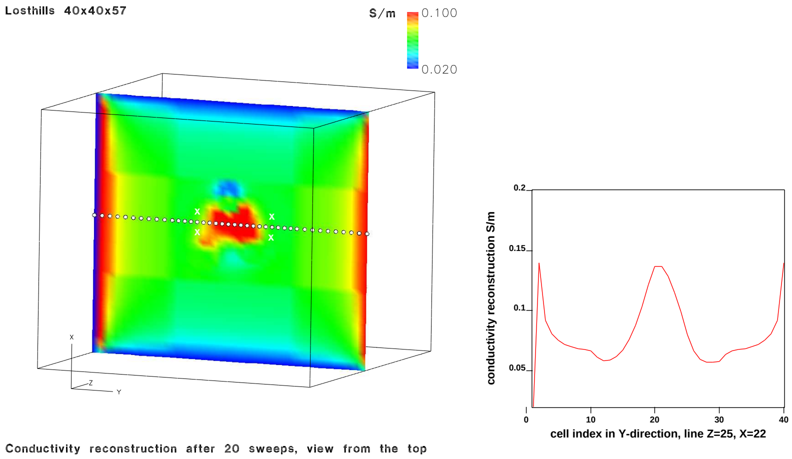

Figure 15: *Left:* The reconstructed conductivity on the same cross-section as in Figure 11, but after 20 sweeps. The conductivity shown here is the sum of the conductivity of the layered background medium, and the accumulated update after 20 sweeps shown in Figure 13. *Right:* cross-section along the line on the left.

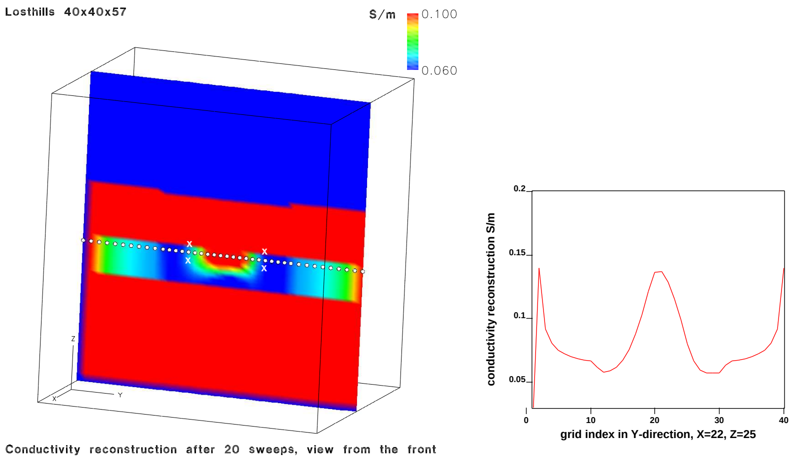

Figure 16: *Left:* The reconstructed conductivity on the same cross-section as in Figure 12, but after 20 sweeps of the adjoint field algorithm. The inclusion is more clearly visible than after only one sweep. The edges of the true inclusion are indicated by an 'X'. *Right:* Plot along the line on the left.

6.4 Numerical experiment recovering two small inclusions

The setup of our second numerical experiment is shown in Figures 5 and 6. Two inclusions having physical size 24mx32mx20m or 4x4x4 grid cells are imbedded in the layer of the Lost Hills model ranging from depth 60m to 80m. They are separated by a part of the background material which has the same size as the two inclusions. The conductivity in the inclusion is 0.2 S/m, and the conductivity in the background layer is 0.06 S/m. All remaining parameters (electric permittivity and magnetic permeability) are the same in the whole domain. Eight boreholes are arranged so that the inclusion is located between them. Each of these boreholes contains three equally spaced z-directed dipole transmitters at depths of 35m,70m,105m below the free surface, with only one active at a time. 17 receivers are arranged equally spaced in each borehole, starting at a depth of 30m and going down to 110m. 64 receivers are equally spaced at the surface of the earth. The magnetic field at the receiver positions is measured, and the aim is to recover the two inclusions given the recorded data. In addition, we want to be able to separate these two inclusions in the reconstruction. This means that, ideally, they should not 'melt together' in the reconstructed conductivity distribution. As initial guess for our iterations we again use the correct layered background material.

We apply filters of radius 15m around the sources and receivers in the boreholes and of radius 45m around the surface detectors. This means that we essentially do not change the conductivity directly below the free surface during the reconstruction process. For this reason we do not include this region in our count of unknowns and data. In this second example, the count of unknowns and data gives about 14400 real numbers as data for the determination of 8000 (without counting the surface-near region) or 11700 (including the surface-near region) real conductivity values, which is more favorable for the reconstruction task than it was in the first example.

In the following we will discuss Figures 17 to 26 one by one. Again, the figures with odd numbers (17,19,...,25) refer to horizontal cross-sections ('view from the top'), whereas figures with even numbers (18,20,...,26) refer to vertical cross-sections ('view from the front').

6.4.1 The true conductivity model

In Figure 17 the Lost Hills model of a layered medium with two separated inclusions is shown on the left. The conductivity inside a layer that contains the two inclusions (70 meters or 14 cells below the free surface.) The view is from the top. The aim in the reconstruction process is to recover and to distinguish between the two inclusions. The eight boreholes are indicated by an 'O', and the edges of the inclusions are indicated by an 'X'. The inner part of the mesh with smaller grid cells models the physical domain of interest, whereas the outer part models the PML. On the right is the plot of the conductivity along the cross-section indicated on the left. The conductivity of the inclusions is 0.2 S/m, imbedded in a background medium with conductivity 0.06 S/m. The outer slopes in the plot are the PML.

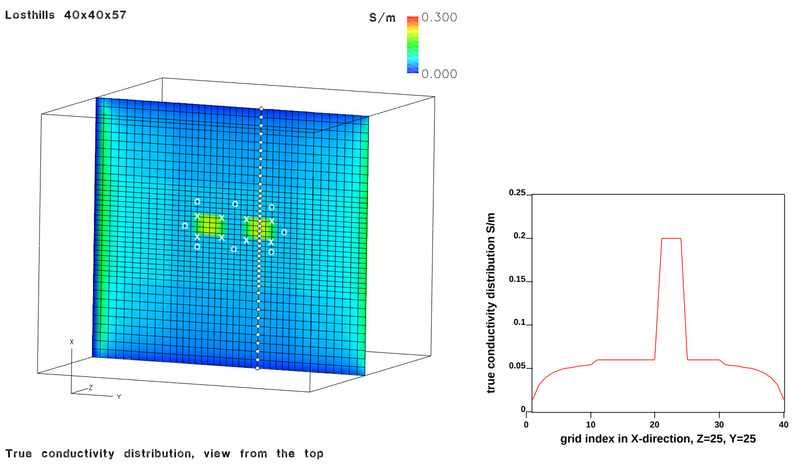

Figure 17: *Left.* Lost Hills model of a layered medium with two separated inclusions. The view is from the top. The eight boreholes are indicated by an 'O', and the edges of the inclusions are indicated by an 'X'. *Right:* Plot of the conductivity along the cross-section shown on the left.

On the left Figure 18 is the same Lost Hills model as in Figure 17. Now the conductivity is displayed in a vertical cross-section with constant X-values (going through the center of the inclusion), which contains the two inclusions. The inner part of the mesh contains the domain of physical interest, and the outer part contains the PML. The part of the mesh colored in dark blue is the layer containing air and the adjacent PML. The layers beneath this dark blue region are soil and rock materials with varying conductivity values (between 0.06 S/m and 0.3 S/m.) The edges of the two inclusions are indicated by an 'X'. On the right side the plot shows the variation of the conductivity over the vertical cross-section indicated on the left. The sharp edges of the original Lost Hills model are smoothed out slightly by the discretization scheme when averaging the parameters over adjacent cells.

6.4.2 One-sweep reconstruction

Figure 19 shows (on the left) the accumulated update of the conductivity after one sweep of the algorithm on the same plane as displayed in Figure 17. The view is from the surface. The figure can alternatively be described as showing the difference between the reconstruction of the conductivity after one sweep and its initial guess, which is the correct layered background conductivity. The edges of the two inclusions are indicated by 'X'. The cross-section on the right is again along the line on the left. The accumulated conductivity update is still quite small after one sweep.

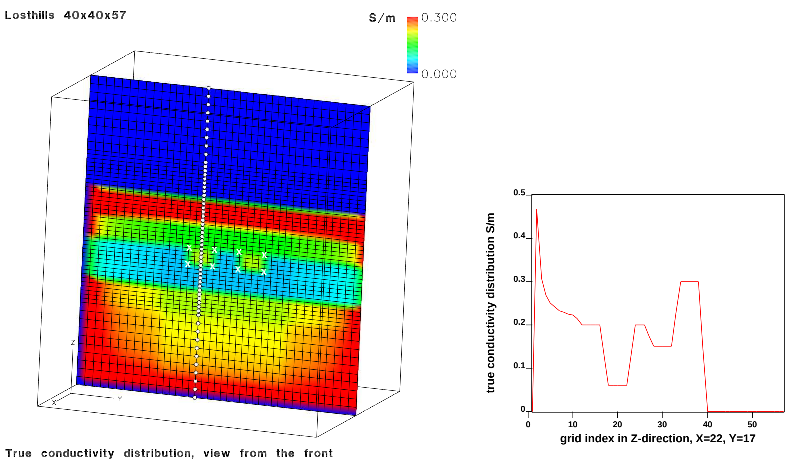

Figure 18: *Left:* The same Lost Hills model as in Figure 17 showing the conductivity in a vertical cross-section of the earth with constant X-values, which contains the two inclusions. The inner part of the mesh is the domain of physical interest, and the outer part is the PML. *Right:* Plot along the line on the left.

However, the two inclusions are already clearly separated at this early stage of the reconstruction.

Figure 20 shows (on the left) the accumulated update of the conductivity after one sweep, on the same vertical cross-section (with constant coordinate X=22) as in Figure 18. The Z-axis in the figure points out of the earth into the air. The edges of the inclusion are indicated by an 'X'. On the right is the accumulated conductivity update along the line on the left. After one sweep, the accumulated update is still small.

Next we consider Figure 21 whose left hand side shows the reconstructed conductivity distribution after one sweep. The view is from the top. This figure displays the sum of the initial conductivity guess and the accumulated update of Figure 19 on the same cross-section. The initial guess is the correct layered background conductivity, including the PML. The conductivity inside the PML is not updated during the reconstruction. The edges of the correct inclusions are indicated by 'X'. The right side is a plot along the line on the left. After one sweep of the algorithm, the contrast between the conductivity of the detected inclusion and the background value is still small.

On the left Figure 22 shows the reconstructed conductivity after one sweep, on the same vertical cross-section with constant X-coordinate (going through the center of the inclusion) as in Figures 18, 20, 24. It is the sum of the conductivity used as

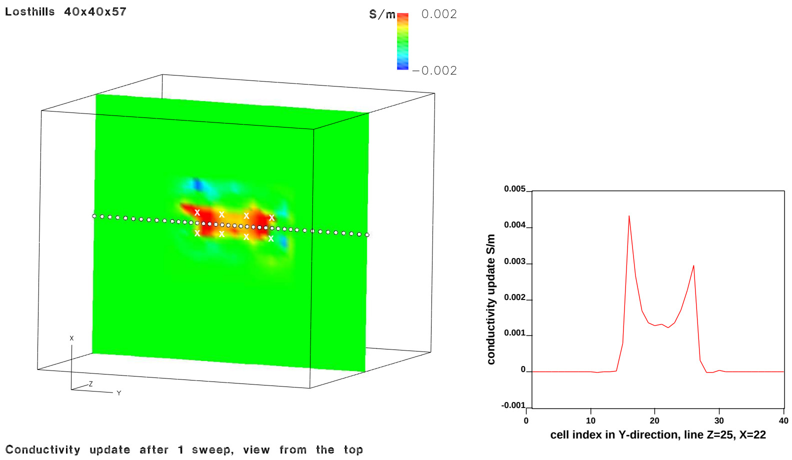

Figure 19: *Left:* The accumulated update of the conductivity after one sweep of the algorithm, on the same plane as in Figure 17. The view is from the top. The edges of the two inclusions are indicated by 'X'. *Right:* Cross-section along the line on the left. The accumulated conductivity update is still quite small after one sweep.

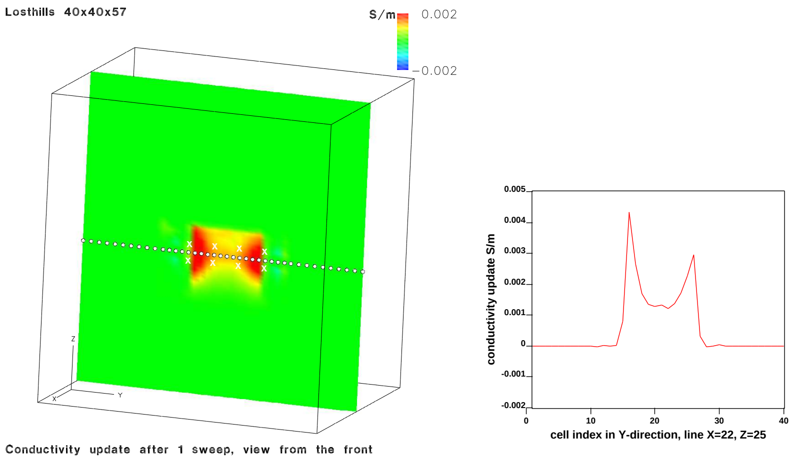

Figure 20: *Left:* Accumulated update of the conductivity distribution after one sweep, shown on the same vertical cross-section (with constant coordinate X=22) as in Figure 18. The edges of the inclusion are indicated by an 'X'. *Right:* Plot of the accumulated conductivity update along the line on the left. After one sweep, the accumulated update is still small.

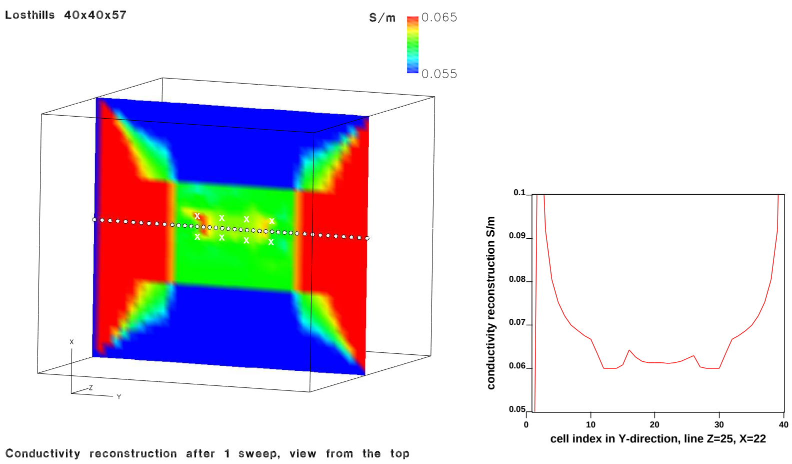

Figure 21: *Left:* Reconstructed conductivity after one sweep. The view is from the top. It is the sum of the initial conductivity guess and the accumulated update of Figure 19 on the same cross-section. *Right:* Plot along the line indicated in the left figure. After one sweep the contrast between the conductivity of the detected inclusions and the background value is still small.

initial guess (the layered background medium) and the accumulated update shown in Figure 20. However, the coloring scheme is different. The contrast of the two detected objects is still very small compared to the contrast between the conductivity of the different layers, so that they are not easily observable. On the right hand side is a plot along the line shown on the left. The detected inclusions have low contrast after one sweep.

6.4.3 Fifteen-sweep reconstruction

On the left Figure 23 shows the accumulated update on the same cross-section as Figure 19, but after 15 sweeps of the adjoint field algorithm. The shapes of the two reconstructed inclusions are now very close to those of the true inclusions (indicated by 'X'), and their positions are recovered very well. The two reconstructed inclusions are now clearly separated from each other. On the right is the accumulated conductivity update along the line indicated on the left. The peak value on this line is 0.1 S/m. This is already close to the true value of 0.14 S/m. The two inclusions are clearly separated from each other.

On the left Figure 24 shows the accumulated update of the conductivity on the same vertical cross-section as in Figure 20, but after 15 sweeps. The edges of the two correct inclusions are indicated by 'X'. The locations of the two reconstructed

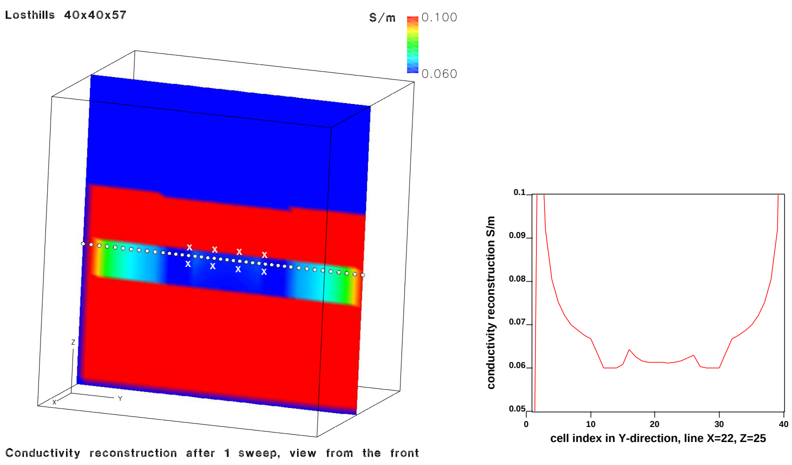

Figure 22: *Left:* Reconstructed conductivity distribution after one sweep shown on the same vertical cross-section with constant X-coordinate (X=22) as in Figures 18,20,24. The contrast of the two detected inclusions is still very small compared to that between the conductivity of the different layers, so that they are not easily observable in this display. *Right:* Plot along the line indicated in the left figure.

inclusions agree very well with the locations of the true inclusions. Also, the shapes of the inclusions are recovered well. Some negative artifacts (blue areas) can be seen at the outer edges of the inclusions, which indicate the dipole character of the elementary updates. Note also the phantom in the reconstruction, which appears between the reconstructed inclusions and the free surface. It is presumably caused by the large number of surface detectors. On the right is plotted the accumulated update along the line shown in the figure to the left. The peak value (0.1 S/m) is close to the true conductivity constrast between the inclusion and the background layer (0.14 S/m).

Finally, in Figure 25, we show the reconstructed conductivity on the same cross-section as in Figure 21, but after 15 sweeps. The conductivity shown is the sum of the conductivity of the layered background medium, and the accumulated update after 15 sweeps shown in Figure 23. The shapes of the two detected inclusions are now close to the true ones (indicated by the 'X'), and the locations are discovered very well. The two inclusions are clearly separated from each other. On the right side is the cross-section along the line indicated in the left. The peak value of this plot (0.15 S/m) is already close to the conductivity of the true inclusion (0.2 S/m).

For comparison with Figure 25, Figure 26 shows the same cross-section of the reconstructed conductivity as in Figure 22, but after 15 sweeps of the adjoint field

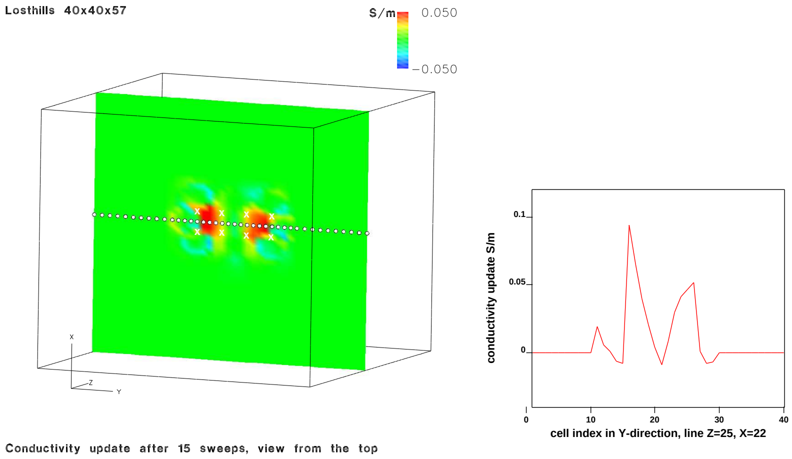

Figure 23: *Left:* The figure shows the same cross-section of the accumulated update as Figure 19, but after 15 sweeps of the adjoint field algorithm. The shapes of the two reconstructed inclusions are now very close to those of the true ones(indicated by ‘X’), and they are now clearly separated from each other. *Right:* Plot along the line indicated in the figure.

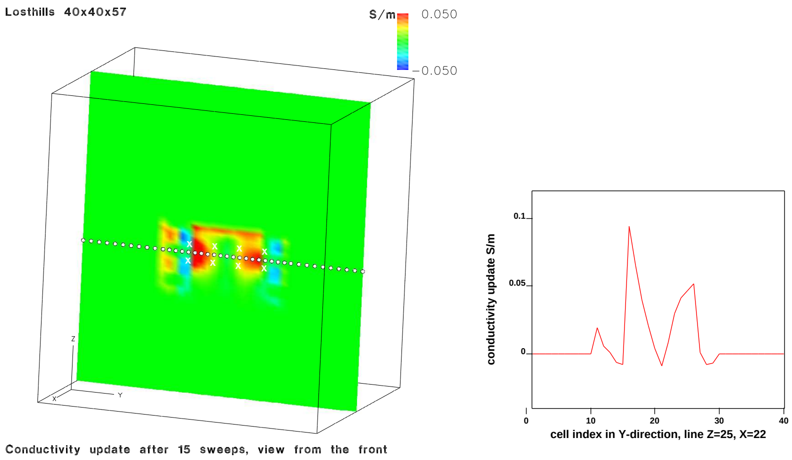

Figure 24: *Left:* The accumulated update of the conductivity on the same vertical cross-section as in Figure 20, but after 15 sweeps. The locations of the two reconstructed inclusions agree very well with those of the true inclusions. Also, the shapes of the inclusions are recovered well. *Right:* Plot of the accumulated update along the line shown in the figure.

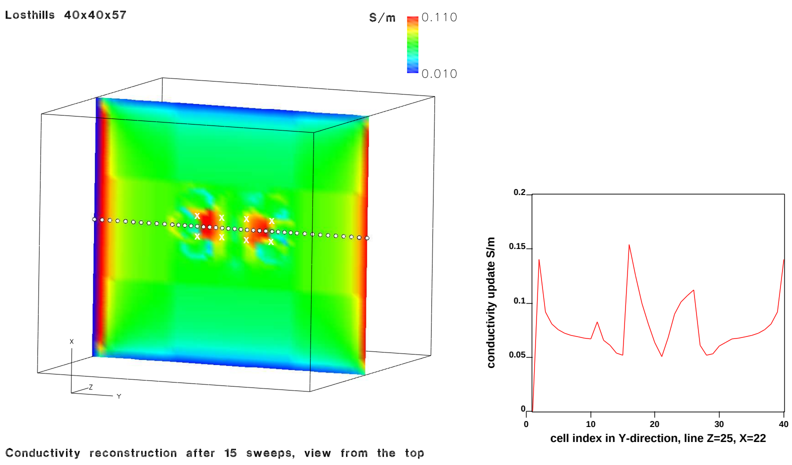

Figure 25: *Left:* The reconstructed conductivity distribution on the same cross-section as in Figure 21, but after 15 sweeps. The shapes of the two detected inclusions are now close to the shapes of the true ones (indicated by the 'X'), and the locations are identified very well. The two inclusions are clearly separated from each other. *Right:* Plot along the line on the left.

algorithm. The coloring scheme has not been changed in order to compare with Figure 22. The two inclusion are more clearly visible than after only one sweep. The edges of the correct inclusions are indicated by 'X'. On the right we have plotted the conductivity along the line on the left. The improvement in the reconstruction between the first and the fifteenth sweep is substantial.

7 Summary and future directions

Our main contributions in this paper are as follows:

We construct fully 3D electromagnetic inversions. We apply a fully functioning PML to deal with infinite space. Both the code and the inversion method are extendable to anisotropic media. The nonlinear inversion method is iterative and is not limited to low contrast as are the Born and Rytov methods. The inversion method is applicable to general, not necessarily layered, media having compact anomalies. Multiple frequencies can be used. The iversion algorithm is fully modular with the EM solver as a stand alone module in both the direct and the adjoint steps.

Some interesting and important issues for future research are:

The effects of noise and modifications needed for use with real field data. The introduction of coarse graining for constructing the matrix AA^* in the minimum

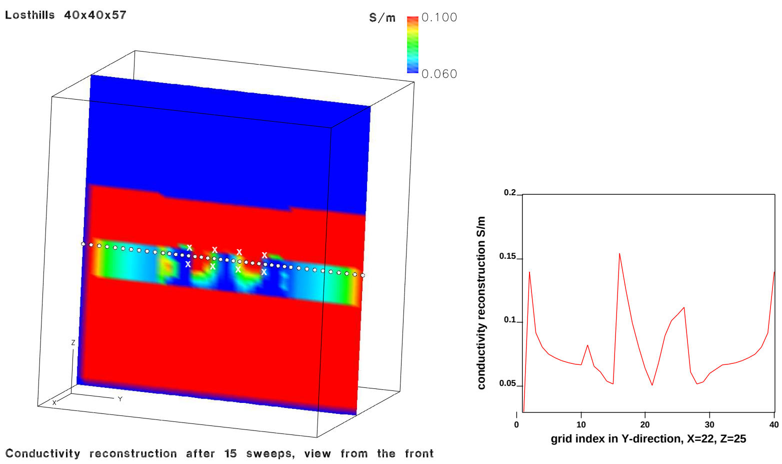

Figure 26: *Left:* The same cross-section of the reconstructed conductivity as in Figure 22, but after 15 sweeps of the adjoint field algorithm. The two inclusion are now more clearly visible than after only one sweep. *Right:* Plot along the line on the left. The improvement in the reconstruction between the first and the fifteenth sweep is clearly visible.

length inversion for underdetermined problems. Analytical studies of convergence of the inversion algorithm. Detailed comparison with Born and Rytov reconstructions.

Acknowledgments

We thank N. J. Champagne (LLNL) for supplying us with the electromagnetics forward modeling code FDFD prior to publication. We thank H. M. Buettner (LLNL) for further assistance with the use of the EM code and for supplying us with the basic Lost Hills model we used in our synthetic examples. Work of OD was performed at Stanford University with partial support from the AFOSR and from the Environmental Management Science Program of DOE. The work of HBA and JGB was performed under the auspices of the U.S. Department of Energy by the Lawrence Livermore National Laboratory under contract No. W-7405-ENG-48 and supported specifically by the Environmental Management Science Program of the Office of Environmental Management and the Office of Energy Research. Work of GCP was supported in part by grant F49620-98-1-0211 from AFOSR and by the NSF, DMS 96228554.

References

[1] Alumbaugh, D. L, and H. F. Morrison, 1995a, Monitoring subsurface changes over time with cross-well electromagnetic tomography, *Geophysical Prospecting* **43**, 873–902.

[2] Alumbaugh, D. L., and H. F. Morrison, 1995b, Theoretical and practical considerations for crosswell electromagnetic tomography assuming cylindrical geometry, *Geophysics* **60**, 846–870.

[3] Beilenhoff, K., W. Heinrich, and H. L. Hartnagel, "Improved finite-difference formulation in frequency domain for three-dimensional scattering problems," *IEEE Trans. Microwave Theory Tech.* **40**, 540–546, 1992.

[4] Berenger, J. P., "A perfectly matched layer for the absorption of electromagnetic waves," *J. Computational Phys.* **114**, 185–200, 1994.

[5] Berryman, J. G., and R. V. Kohn, 1990, Variational constraints for electrical impedance tomography, *Phys. Rev. Lett. 65*, 325–328.

[6] Borcea, L., 1996, *Direct and Inverse Problems for Transport in High Contrast Media*, Ph.D. thesis, Stanford University, May, 1996.

[7] Borcea, L., J. G. Berryman, and G. C. Papanicolaou, 1999, Matching pursuit for imaging high contrast conductivity, *Inverse Problems* **15**, 811–849.

[8] Buettner, H. M., and J. G. Berryman, An electromagnetic induction tomography field experiment at Lost Hills, CA, in the *Proceedings of SAGEEP*, Oakland, CA, March 14–18, 1999, pp. 663–672.

[9] Champagne, N. J., II, J. G. Berryman, H. M. Buettner, J. B. Grant, and R. M. Sharpe, A finite-difference frequency-domain code for electromagnetic induction tomography, in the *Proceedings of SAGEEP*, Oakland, CA, March 14–18, 1999, pp. 931–940.

[10] Colton, D., and Paivarinta, L.: The uniqueness of a solution to an inverse scattering problem for electromagnetic waves, *Arch. Rat. Mech. Anal.* **119**, (1992), pp. 59–70.

[11] Claerbout, J. F., 1976, *Fundamentals of Geophysical Data Processing: With Applications to Petroleum Prospecting*, McGraw-Hill, New York.

[12] Daily, W. D., A. Ramirez, D. LaBrecque, and J. Nitao, 1992, Electrical resistivity tomography of vadose water movement, *Water Resources Res.* **28**, 1429–1442.

[13] Davis, J.L., and A. P. Annan, 1989, Ground penetrating radar for high resolution mapping of soil and rock stratigraphy, *Geophysical Prospect.* **37**, 531–551.

[14] Dines, K.A., and R.J. Lytle, 1979, Computerized geophysical tomography, *Proc. IEEE*, **67**, 1065–1073.

[15] Dorn, O., Das inverse Transportproblem in der Lasertomographie, *Thesis. Preprints Angewandte Mathematik und Informatik* 7/97-N, University of Münster (1997).

[16] Dorn, O., A transport-backtransport method for optical tomography, *Inverse Problems* **14** (1998) 1107–1130.

[17] Fisher, E., G. A. McMechan, and A. P. Annan, 1992, Acquisition and processing of wide-aperature ground penetrating radar data, *Geophysics* **57**, 495–504.

[18] Habashy, T. M., R. W. Groom, and B. R. Spies, 1993, Beyond the Born and Rytov approximations: A nonlinear approach to electromagnetic scattering, *J. Geophys. Res.* **98**, 1759–1775.

[19] Kuzuoglu, M., and R. Mittra, "Frequency dependence of the constitutive parameters of causal perfectly matched anisotropic absorbers," *IEEE Microwave Guided Wave Lett.* **6**, 447–449, 1996.

[20] Natterer F. (1986) *The Mathematics of Computerized Tomography* (Stuttgart: Teubner)

[21] Natterer F., and Wübbeling F. (1995) A propagation-backpropagation method for ultrasound tomography *Inverse Problems* **11** 1225–1232

[22] Natterer, F. (1996) Numerical Solution of Bilinear Inverse Problems *Preprints* "Angewandte Mathematik und Informatik" 19/96-N Münster

[23] Newman, G. A., and D. L. Alumbaugh, 1997, Three-dimensional massively parallel electromagnetic inversion I. Inversion, *Geophys. J. Int.* **128**, 345–354.

[24] Ola, P., Paivarinta, L., and Somersalo, E.: An inverse boundary value problem in electrodynamics, *Duke Math. J.* **70** (3), (1993), pp. 617–653.

[25] Ramirez, A., W. D. Daily, D. LaBrecque, E. Owen, and D. Chesnut, 1993, Monitoring an underground steam injection process using electrical resistance tomography, *Water Resources Res. 29*, 73–87.

[26] Romanov, V.G. and S.I. Kabanikhin, *Inverse Problems for Maxwell's Equations*, Inverse and Ill-posed Problems Series, VSP, Utrecht, 1994.

[27] Sacks, Z. S., D. M. Kingsland, R. Lee, and J. F. Lee, A perfectly matched anisotropic absorber for use as an absorbing boundary condition, *IEEE Trans. Antennas Prop.* **43**, 1460–1463, 1995.

[28] Somersalo, E., Isaacson, D., and Cheney, M.: A linearized inverse boundary value problem for Maxwell's equations, *J. Comp. Appl. Math.* **42**, (1992), pp. 123–136.

[29] Spies, B. P., and T. M. Habashy, Sensitivity analysis of crosswell electromagnetics, *Geophysics* **60**, 834–845 (1995).

[30] Sun, Z., Uhlmann, G.: An inverse boundary value problem for Maxwell's Equations, *Arch. Rat. Mech. Anal.* **119**, (1992), pp. 71–93.

[31] van der Vorst, H. A., "Bi-CGSTAB: A fast and smoothly converging variant of Bi-CG for the solution of non-symmetric linear systems," *SIAM J. Sci. Stat. Comput.* **12**, 631–644, 1992.

[32] Ward, S. H., and G. W. Hohmann, Electromagnetic theory for geophysical applications, in *Electromagnetic Methods in Applied Geophysics – Theory*, Vol. 1, M. N. Nabighian (ed.), SEG, Tulsa, Oklahoma, 1987, p. 131–311.

[33] Wilt, M. J., D. L. Alumbaugh, H. F. Morrison, A. Becker, K. H. Lee, and M. Deszcz-Pan, 1995a, Crosswell electromagnetic tomography: System design considerations and field results, *Geophysics* **60**, 871–885.

[34] Wilt, M.J., H. F. Morrison, A. Becker, H.-W. Tseng, K. H. Lee, C. Torres-Verdin, and D. Alumbaugh, 1995b, Crosshole electromagnetic tomography: A new technology for oil field characterization, *The Leading Edge* **14**, March, 1995, pp. 173–177.

[35] Wilt, M. J., C. Schenkel, M. Wratcher, I. Lambert, C. Torres-Verdin, and H.-W. Tseng, 1996, Crosshole EM for oil field characterization and EOR monitoring: Field examples from Lost Hills, California, LLNL UCRL-ID-123893, July 16, 1996.

[36] Wu, J. Y., D. M. Kingsland, J. F. Lee, R. Lee, "A comparison of anisotropic PML to Berenger's PML and its application to the finite-element method for EM scattering," *IEEE Trans. Antennas Propagat.* **45**, 40–50, 1997.

[37] Zhdanov, M. S., P. Traynin, and J. R. Booker, 1996, Underground imaging by frequency-domain electromagnetic migration, *Geophysics* **61**, 666–682.

[38] M. Zhdanov and H. Bertete-Aguirre, Electromagnetic modeling in a medium with a vertical axis of symmetry, CEMI annual meeting, University of Utah, (1996).